# A KDE-based non-parametric cloud approach for efficient seismic fragility estimation of structures under non-stationary excitation

Xu-Yang Cao[a], De-Cheng Feng[b,*], Michael Beer[c,d,e]

[a]College of Civil and Transportation Engineering, Hohai University, Nanjing 210098, China
[b]Key Laboratory of Concrete and Prestressed Concrete Structures of the Ministry of Education, Southeast University, Nanjing 210096, China
[c]Institute for Risk and Reliability, Leibniz University Hannover, Callinstr. 34, Hannover, Germany
[d]Institute for Risk and Uncertainty, University of Liverpool, Peach Street, L69 7ZF Liverpool, United Kingdom
[e]International Joint Research Center for Engineering Reliability and Stochastic Mechanics, Tongji University, Shanghai 200092, China

**Abstract**

With the development of performance-based earthquake engineering, the risk-informed assessment framework has received broad recognition over the world, of which the probability seismic fragility analysis is an important step. The classic seismic fragility adopts the lognormal assumption and forms a parametric derivation. With the development of fragility theory, researchers are hoping to seek out non-parametric approaches to express the intrinsic fragility in a pure analytical form without any distribution assumptions. Besides, how to keep the calculation efficiency (e.g., combining with cloud approach) and how to consider the non-stationary stochastic responses (e.g., combining with non-stationary stochastic excitation model) are critical aspects in fragility that deserve further attention of researchers. In this paper, a kernel density estimation (KDE) based non-parametric cloud approach is proposed for efficient seismic fragility estimation of structures under non-stationary excitation. First, the methodology framework of the efficient approach is illustrated. Then, the procedures of non-stationary stochastic seismic response of structures and KDE-based non-parametric cloud approach for efficient seismic fragility are demonstrated. After that, an application example via a three-span-six-story reinforced concrete frame is given for implementation, followed with a parametric analysis of critical factors. During the process, the classic parametric linear-regression based cloud approach (cloud-LR) and benchmark Monte-Carlo-simulation based cloud approach (cloud-MCS) are also incorporated for validation. In general, the analysis verifies the effectiveness of the non-parametric cloud-KDE approach without requiring more computation work (i.e., same as the parametric cloud-LR approach and much less than the benchmark cloud-MCS approach). Meanwhile, the non-parametric cloud-KDE approach indicates a comparable accuracy with the classic fragility approaches (i.e., less deviation than the parametric cloud-LR approach and much closer to the benchmark cloud-MCS approach), and with the increase of stochastic cloud-point number, the corresponding fitting degree of cloud-KDE approach is growing better. The research provides a new sight for the development of non-parametric seismic fragility approach, and the corresponding findings can be further combined with the probabilistic hazard and risk analysis for a non-parametric assessment procedure in performance-based earthquake engineering.

*Keywords:*
Non-stationary stochastic response, Seismic fragility, Non-parametric, Gaussian-kernel, Cloud-KDE analysis, Probabilistic performance

*Corresponding author.
*Email addresses:* caoxy@hhu.edu.cn (Xu-Yang Cao), dcfeng@seu.edu.cn (De-Cheng Feng), beer@irz.uni-hannover.de (Michael Beer)

*October 8, 2023*

## 1. Introduction

Performance-based earthquake engineering (PBEE) is an emerging theoretical framework that strives to transcend the traditional design methods and to address structural issues from the perspective of structural safety, functionality, and economics for all investors [1, 2, 3, 4, 5, 6]. At this stage, it has become a research hot issue and future development direction in the field of earthquake engineering over the world. The PBEE develops with the times, and nowadays the risk-informed PBEE framework has received broad recognition. Cornell et al. [7] first proposed the risk-based PBEE procedure, and during the process the fully probability-based theory is well incorporated. At this stage, the risk-informed PBEE framework primarily focuses on the risk assessment of the concerned physical object (e.g., loss, maintenance, reparability), and it commonly involves three important links (i.e., probabilistic seismic hazard analysis, probabilistic seismic fragility analysis, and probabilistic seismic risk analysis), among which the probabilistic seismic fragility analysis is the most critical step that has formed a connecting link between the preceding and the following steps [8, 9, 10, 11, 12, 13]. With the accurate seismic fragility assessments, the subsequent construction strategies for new structures and retrofitting approaches for aged structures can be appropriately given [14, 15, 16, 17, 18, 19, 20].

The probabilistic seismic fragility reflects the exceeding probability of structures under earthquake for a specific limit state, and it depicts the uncertain performance of structures between the demand and capacity from a probabilistic perspective [21, 22, 23, 24, 25, 26, 27]. The accuracy of fragility is largely affected by the adopted earthquake excitations and spectral features. Commonly, the earthquakes are selected from the database according to the local site conditions, fortification level as well as the target spectra [28, 29, 30, 31]. However, according to Chopra [32], historical data have proved that earthquakes possess lots of randomness, and even under the same site, the potential earthquakes in the adjacent time periods may have different spectral features. In another word, the selected earthquakes from the database may not appropriately characterize the potential hazards and seismic properties of the target regions. Against this background, the stochastic earthquake model is proposed by researchers, and the stochastic theory is adopted to treat the whole earthquake excitation process as a stochastic process. The stochastic earthquake model commonly contains a series of random functions and variables (e.g., power spectral density function, phase angle function, intensity modification function), and the corresponding values are randomly generated in terms of the stochastic process theory as well as the target site characteristics. Kaul [33] modelled the earthquake as a stochastic process, and the corresponding stochastic characterization as well as the extreme values were well captured through response spectrum. Both the approximate scheme and iterative scheme were given after connecting the power spectral density with the response spectrum, which verified the significance of the stochastic process to characterize the earthquake input. Rezaeian and Kiureghian [34] presented a generating approach for stochastic ground motion via a modulated and filtered white noise process. A series of parameters were included (i.e., evolving intensity, fundamental frequency, acceleration bandwidth), and the proposed approach was proved to be superior for dynamic analysis of engineering system in comparison with the pure recorded earthquakes. Scozzese et al. [35] employed a stochastic ground motion model to perform the multiple stripe assessments during the probabilistic seismic fragility analysis. The stochastic ground motion model was well compared with the traditional earthquake approaches, which gave useful insights for the stochastic structural dynamic evaluation.

Apart from this, the early stochastic earthquake model generally adopts the stationarity assumption and ignores the time-varying effects of earthquake excitations. For an instance, the stationary stochastic earthquake model generally takes the power spectrum as a constant or takes the frequency parameter as a constant, but does not treat as a time-varying variable. With the further development of the stochastic earthquake model, researchers found that the non-stationary property of earthquake is a quite significant aspect and may obviously affect the structural response after excitation (e.g., in space, frequency and intensity) [36, 37, 38, 39, 40, 41]. Amin and Ang [42] first proposed the non-stationary stochastic earthquake model, and proved the importance of non-stationary random process in earthquake modelling. During the process, a second-order Gaussian-induced non-stationary process with shot-noise was well proposed, which laid a significant basis for the future research. Srinivasan et al. [43] proposed a critical non-stationary stochastic earthquake model, and a filtered shot-noise procedure was well incorporated for implementation.

Both the frequency non-stationarity and time non-stationarity were given in response statistics, and its sensitivity to pulse-arrival rate was also well compared with the recorded strong earthquakes. Conte and Peng [44] further developed the non-stationary stochastic earthquake model and proposed an intensity-frequency non-stationary form (i.e., fully non-stationarity). Two actual records were adopted for validation based on the second order statistics, and the results proved the accuracy and applicability of the fully non-stationary form. Besides, Stewart et al. [45], Mavroeidis and Papageorgiou [46], Jalayer and Beck [47], Gidaris et al. [48], and Kwong et al. [49] also made great contributions to the development of stochastic earthquake generation and non-stationary dynamic property in the corresponding field.

Another factor that obviously affects the accuracy of fragility is the fragility assumption and calculation approach. At this stage, the most commonly adopted approach is by introducing the lognormal assumption of random variables [50, 51, 52], i.e. Eq. 1, in which $C$ and $D$ represent the structural capacity and seismic demand, respectively, and the two random variables are both lognormally distributed. $S_{d|IM}$ and $S_c$ represent the seismic demand median and structural capacity median, respectively, and $ln(\beta_{d|IM})$ and $ln(\beta_c)$ represent the logarithmic standard deviation of seismic demand and structural capacity, respectively. Commonly, the strategies to obtain the demand-to-capacity pairs include the incremental dynamic analysis, multiple stripe analysis, or cloud analysis, and the strategies to obtain the above-mentioned coefficients include the least squares regression, maximum likelihood estimation or safety factor method [53, 54].

$$P\left[D > C|IM\right] = \Phi\left[ln(S_{d|IM}/S_c)/\sqrt{ln(\beta_{d|IM})^2 + ln(\beta_c)^2}\right] \tag{1}$$

The lognormal-based assumption is classic in seismic fragility and has been widely recognized. It is also a parametric approach relying on the accurate values of the above-mentioned coefficients [i.e., $S_{d|IM}$, $S_c$, $ln(\beta_{d|IM})$ and $ln(\beta_c)$]. Nielson and DesRoches [55] proposed an expanded approach to generate the seismic fragility of highway bridges, and the approach was directly correlated to the individual components of bridges. The research found that the bride system was more fragile in comparison with the individual components. Ghosh and Padgett [56] developed the time-dependent seismic fragility curves and incorporated the aging-deterioration factors into the analysis framework. The changes of lognormal-based parameters were also proposed in fragility expression, and the research indicated a 32 % shift in the fragility medians for the complete-damage state. Zentner et al. [57] performed a comprehensive review of the lognormal-based fragility approaches in the nuclear industry, including the safety factor, regression analysis, maximum likelihood estimation, and incremental dynamic analysis. The characteristics of these approaches were well compared and the corresponding impacts in the lognormal assumptions were well evaluated. Bakalis and Vamvatsikos [58] gave an elaborative generating procedure of lognormal-based seismic fragility through the nonlinear dynamic results, and all the necessary information involved was well discussed. The incremental dynamic analysis was combined during the whole process, and the effects of response coefficients as well as intensity measures were comprehensively outlined. Besides, lognormal-based approaches have been broadly used into various civil infrastructures [59, 60, 61, 62] and have presented an important role in structural performance assessment.

Although the lognormal-based assumption in seismic fragility shows huge superiority, it also indicates some limitations. According to Karamlou et al. [63], the lognormal-based assumption may lose certain accuracy when the real material-geometric nonlinearity of environment is considered. Bradley et al. [64] found that the effectiveness of lognormal-based assumption is dropped due to the collapsing cases of structures, especially when the seismic intensity is in a large level. Mangalathu and Jeon [65] also got the similar findings that the lognormal-based assumption may lead to unrealistic fragility results under the multivariate coupling conditions. Moreover, the lognormal-based assumption is ideally parametric, which means that the obtained fragility is sensitive to the assumed parameters. However, the true fragility value should be linked to the intrinsic characteristics of structural system while not to the assumed parameters in calculation. Thus, researchers are hoping to seek out a non-parametric approach to express the seismic fragility in recent years [66, 67, 68]. Lallemant et al. [69] discussed the statistical procedures for seismic fragility curves and compared the limitations between the parametric models and non-parametric models (i.e., Gaussian kernel smoothing model and generalized additive model). The research also analyzed the applicability and accuracy of various fragility approaches for the further selections. Trevlopoulos et al. [70]

proposed an enhanced Monte Carlo procedure to calculate the non-parametric structural fragility. The data of intensity measure were clustered via an enriched earthquake database, and the classic parametric models were averaged for optimized evaluation. The results of non-parametric approach indicated a smaller confidence interval and a satisfactory estimation even with 100 dynamic calculations. Gentile and Galasso [71] proposed a non-parametric fragility approach for structural assessment, and during the procedure, the surrogate model was well combined by means of the Gaussian-based regressions. The results revealed that the non-parametric approach possessed an accurate predicting capacity in structural performance, which proved the feasibility in practice and the potentials for further decision making. Altieri and Patelli [72] developed a non-parametric approach to perform the analytical seismic fragility of structures. During the procedure, the subsets were identified, the failure region was mapped, and the generated samples were associated with the classification score for fragility calculation. The proposed method also avoided the rare failure domains in the existing parametric methods. Moreover, Jalayer and Cornell [73], Naess [74], Echard et al. [75], Baker [76], Mangalathu et al. [77], Lee [78], Ghosh et al. [79] and Iervolino [80] also contributed greatly to the field of non-parametric fragility approaches and their researches have provided a solid basis for the subsequent explorations.

It can be concluded from the above reference review that the non-stationary stochastic responses of structures reflect the stochastic properties and time-varying effects of earthquake excitations, and the adoption of non-stationary stochastic earthquake can be a more objective strategy for seismic fragility assessment of engineering structures. Meanwhile, although the lognormal-based assumption in seismic fragility is classic, it also indicates some limitations and constraints in actual analysis, thus a non-parametric approach to express the intrinsic seismic fragility may be more objective and real. At this stage, although a series of non-parametric approaches are developing, the kernel density estimation (KDE) based approach is unique and superior for its pure analytical expression of fragility without any distribution assumptions [81]. Most importantly, compared with the other non-parametric approaches that commonly require the same or even more number of samples in analysis as the classic parametric approach, the KDE-based fragility approach indicates a great potential to connect with the cloud analysis approach in sample generations (i.e., cloud-KDE), which sharply reduces the calculating burdens and improves the analyzing efficiency. However, at this stage, the framework for non-stationary stochastic seismic fragility assessment of structures via the non-parametric cloud-KDE approach has little implementation.

In this paper, a KDE-based non-parametric cloud approach is proposed for efficient seismic fragility estimation of structures under non-stationary excitation. First, the methodology framework of the efficient approach is illustrated. Then, the procedures of non-stationary stochastic seismic response of structures and KDE-based non-parametric cloud approach for efficient seismic fragility are demonstrated. After that, an application example via a three-span-six-story reinforced concrete frame (RCF) is given for implementation, followed with a parametric analysis of critical factors. During the process, the classic parametric linear-regression based cloud approach (cloud-LR) and benchmark Monte-Carlo-simulation based cloud approach (cloud-MCS) are also incorporated for validation. In general, the analysis verifies the effectiveness of the non-parametric cloud-KDE approach without requiring more computation work (i.e., same as the parametric cloud-LR approach and much less than the benchmark cloud-MCS approach). Meanwhile, the non-parametric cloud-KDE approach indicates a comparable accuracy with the classic fragility approaches (i.e., less deviation than the parametric cloud-LR approach and much closer to the benchmark cloud-MCS approach), and with the increase of stochastic cloud-point number, the corresponding fitting degree of cloud-KDE approach is growing better. The research provides a new sight for the development of non-parametric seismic fragility approach, and the corresponding findings can be further combined with the probabilistic hazard and risk analysis for a non-parametric assessment procedure in performance-based earthquake engineering. The detailed contents and implementary principles are introduced in the following sections.

## 2. Methodology framework

This section introduces the methodology framework of the KDE-based non-parametric cloud approach for efficient seismic fragility estimation of structures under non-stationary excitation, and Fig. 1 presents the schematic view of the specific procedure. In general, the methodology framework is consisted of two major parts, i.e., (1) Non-stationary stochastic seismic response of structures; and (2) KDE-based non-parametric cloud approach for efficient seismic fragility. In the first part of the framework, the stochastic parameters of structures and earthquakes (e.g., material, load, and phase angle) are first determined. Then, the number of earthquake for each intensity bandwidth and for the subsequent cloud-based probabilistic seismic fragility analysis (PSFA) is determined. After that, the total cloud points for PSFA (i.e., number of structural models and non-stationary earthquakes) are obtained, and the Latin hypercube sampling (LHS) is adopted to generate the samples of stochastic parameters. With the generated parameters, the stochastic structural numerical models for PSFA are established based on the numerical softwares, and the non-stationary stochastic earthquakes for PSFA are also established based on the stochastic process theory as well as the spectral representation theory. The deterministic time-history analysis is performed to acquire the engineering demand parameter (EDP), and the intensity measure (IM) of the generated non-stationary stochastic earthquakes is also calculated, with which the stochastic cloud points for PSFA are then formed. In the second part of the framework, the first important step is to calculate the optimal one-dimensional bandwidth of IM (i.e., via the recommended equation in Sec. 4) and the optimal two-dimensional bandwidth between EDP and IM (i.e., via the R procedure in Sec. 4). Then, the marginal probability density function (PDF) and the marginal cumulative distribution function (CDF) of IM are calculated via the one-dimensional Gaussian KDE approach, and the joint-PDF between EDP and IM is calculated via the two-dimensional Gaussian KDE approach. After that, the joint-PDF is integrated from the threshold of EDP to the $+\infty$ under all the IM levels (i.e., joint-CDF), and the results are further combined with the marginal PDF to derive the PSFA via the non-parametric cloud-KDE approach. During the process, the classic parametric cloud-LR approach and the benchmark cloud-MCS approach are also incorporated for comparison and validation. The cloud-LR approach is the most-commonly adopted parametric strategy for seismic fragility in light of the lognormal assumption, and its analytical expression is given in Eq. 1. The cloud-MCS approach is a non-parametric approach which requires mass statistical data, and it is commonly used as a benchmark for validation of unknown variable. The obtained PSFA results of all the cloud-KDE, cloud-LR and cloud-MCS approaches are discussed and analyzed correspondingly. Besides, if the number of cloud points lowers than the required number, the number is then increased for a repeated analysis, and if the number of cloud points exceeds the required number, the analysis is ended and the procedure is finished. More details and specific equations of the methodology framework are displayed in the following section.

## 3. Non-stationary stochastic seismic response of structures

Without the loss of generality, an engineering system is commonly assumed to include diverse stochastic structural variables [e.g., geometry sizes, material strength, construction quality, herein reflected as $\boldsymbol{\Delta_s} = (\boldsymbol{\Delta}_1, \boldsymbol{\Delta}_2, ..., \boldsymbol{\Delta}_x)^T$] and diverse stochastic force variables [e.g., phase angles, force points, temperature stresses, herein reflected as $\boldsymbol{\Delta_f} = (\boldsymbol{\Delta}_{x+1}, \boldsymbol{\Delta}_{x+2}, ..., \boldsymbol{\Delta}_n)^T$]. Then, the systematic stochastic variable $\boldsymbol{\Delta} = (\boldsymbol{\Delta}_s, \boldsymbol{\Delta}_f)$ is given, which contains $n$ groups of mutually independant sub-matrices $(e \times 1)$, where $e$ represents the sample number for every stochastic variable. Based on this, the dynamic balance equation for an arbitrary engineering system and a realizable stochastic variable condition $(\boldsymbol{\Delta})$ can be given as Eq. 2:

$$\boldsymbol{Q_1} \cdot \ddot{\boldsymbol{G}}(\boldsymbol{\Delta}, t) + \boldsymbol{Q_2} \cdot \dot{\boldsymbol{G}}(\boldsymbol{\Delta}, t) + \boldsymbol{Q_3} \cdot \boldsymbol{G}(\boldsymbol{\Delta}, t) = -\boldsymbol{Q_1} \cdot \ddot{g_{ip}}(\boldsymbol{\Delta}, t) \tag{2}$$

in which the mass, damping and stiffness matrices of the engineering system are expressed as $\boldsymbol{Q_1}$, $\boldsymbol{Q_2}$ and $\boldsymbol{Q_3}$, respectively. Meanwhile, the acceleration, velocity and displacement matrices of the engineering system are expressed as $\ddot{\boldsymbol{G}}(\boldsymbol{\Delta}, t)$, $\dot{\boldsymbol{G}}(\boldsymbol{\Delta}, t)$ and $\boldsymbol{G}(\boldsymbol{\Delta}, t)$, respectively. The dimensions of $\boldsymbol{Q_1}$, $\boldsymbol{Q_2}$ and $\boldsymbol{Q_3}$ are $e \times e$, and the dimensions of $\ddot{\boldsymbol{G}}(\boldsymbol{\Delta}, t)$, $\dot{\boldsymbol{G}}(\boldsymbol{\Delta}, t)$ and $\boldsymbol{G}(\boldsymbol{\Delta}, t)$ are $e \times 1$, respectively. $\ddot{g_{ip}}(\boldsymbol{\Delta}, t)$ denotes the non-stationary stochastic earthquake as external excitation. The systematic uncertainties in Eq. 2 are incorporated into the stochastic variable $\boldsymbol{\Delta}$, and $\boldsymbol{G}(\boldsymbol{\Delta}, t)$ embodies the non-stationary stochastic seismic response of the engineering system for any concerned physical object (e.g., maximum inter-story drift, maximum inter-story force, energy coefficient), depending on each $\boldsymbol{\Delta}$ from a broad perspective [82].

The non-stationary stochastic earthquake $[\ddot{g_{ip}}(\boldsymbol{\Delta}, t)]$ commonly contains the frequency non-stationarity and intensity non-stationarity, and it is commonly generated in light of the stochastic process theory as

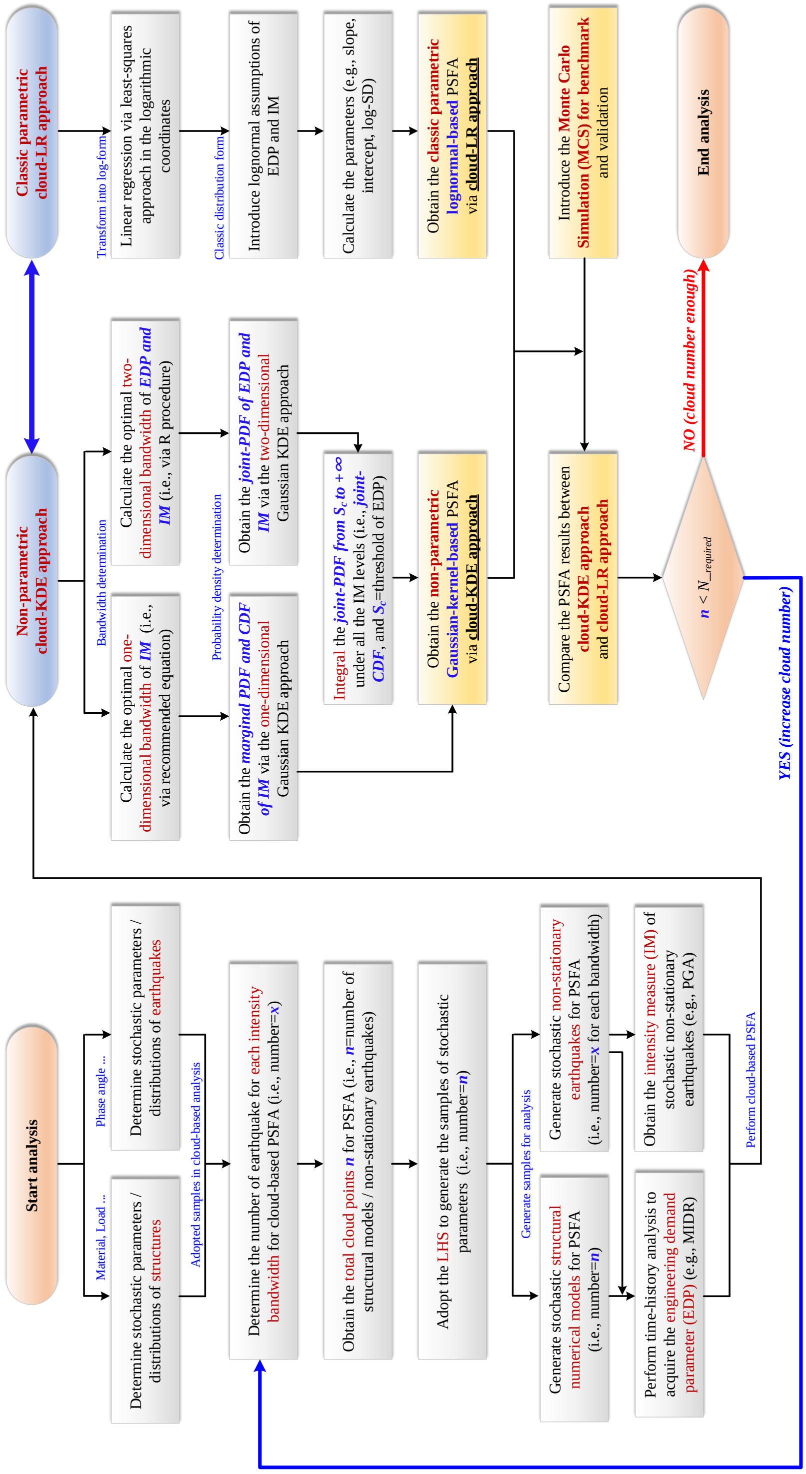


Figure 1: The methodology framework of the non-stationary stochastic cloud-KDE approach for fragility assessment

well as the spectral representation of stochastic functions. The non-stationary stochastic earthquake is believed to better reflect the stochastic characteristics of earthquake excitation and generally indicates a more advantageous analyzing accuracy in performance evaluation [83, 84, 85]. In this paper, the bilateral evolutionary power spectral density (EPSD) function is adopted for stochastic earthquake generation, and during the process the Clough-Penzien model is introduced, which reflects the non-stationary properties of both frequency and intensity [86]. Eq. 3 presents the generation procedure of non-stationary stochastic earthquake $[\ddot{g_{ip}}(\boldsymbol{\Delta}, t)]$, in which the required number of stochastic variables is $2N_{tr}$ (i.e., $\boldsymbol{\Delta}1_k$ and $\boldsymbol{\Delta}2_k, k = 1, 2, ..., N_{tr}$) [87]:

$$\ddot{g_{ip}}(\boldsymbol{\Delta}, t) = \sum_{k=1}^{N_{tr}} \sqrt{2S_{\ddot{g_{ip}}}(t, \beta_k) \cdot \beta_{if}} \cdot \Big[ \cos(\beta_k t) \cdot \boldsymbol{\Delta}1_k + \sin(\beta_k t) \cdot \boldsymbol{\Delta}2_k \Big] \tag{3}$$

in which $\beta_k = k \cdot \beta_{if}$, and $\beta_{if}$ indicates the interval frequency that is related to the truncated items ($N_{tr}$) and truncated frequency ($\beta_c$). $\{\boldsymbol{\Delta}1_k, \boldsymbol{\Delta}2_k\}$ ($k = 1, 2, ..., N_{tr}$) denotes the standard orthogonal stochastic variables, and it is worth noticing that $\{\boldsymbol{\Delta}1_k, \boldsymbol{\Delta}2_k\}$ should be obtained through a stochastic mapping from two sets of the same stochastic variables $\{\boldsymbol{\Psi}1_n, \boldsymbol{\Psi}2_n\}$ ($n = 1, 2, ..., N_{tr}$), as shown in Eq. 4. In a certain sense, the stochastic mapping can be regarded to be a constraint to reasonably reduce the difficulty in dynamic analysis and to effectively guarantee the stochastic characteristics in the generation process [88].

$$\boldsymbol{\Delta}1_k = \boldsymbol{\Psi}1_n,\ \boldsymbol{\Delta}2_k = \boldsymbol{\Psi}2_n,\ k\ or\ n = 1, 2, ..., N_{tr} \tag{4}$$

Through this operation, the generated non-stationary stochastic earthquake avoids the discontinuous amplitude and ensures the ideal time-history process. Eq. 5 indicates the Gaussian-oriented orthogonal form of $\{\boldsymbol{\Psi}1_n, \boldsymbol{\Psi}2_n\}$ based on two independent stochastic phase angles ($P_1$ and $P_2$). Both $P_1$ and $P_2$ conform to the uniform distribution form (ranging from 0 to $2\pi$) and are independent mutually. The total number of stochastic variables during the generation process is sharply reduced after the stochastic mapping, and the dynamic analysis efficiency of the stochastic engineering system is obviously improved from a macro perspective [89].

$$\begin{aligned} \boldsymbol{\Psi}1_n &= \Phi^{-1}\left[\frac{1}{\pi} arcsin(\frac{sin(n \cdot P_1) + cos(n \cdot P_1)}{\sqrt{2}}) + \frac{1}{2}\right],\ n = 1, 2, ..., N_{tr} \\ \boldsymbol{\Psi}2_n &= \Phi^{-1}\left[\frac{1}{\pi} arcsin(\frac{sin(n \cdot P_2) + cos(n \cdot P_2)}{\sqrt{2}}) + \frac{1}{2}\right],\ n = 1, 2, ..., N_{tr} \end{aligned} \tag{5}$$

in which $\Phi$ denotes the standard normal distribution function, and $arc$ denotes the inverse function. The most critical step in the generating procedure depends on the adopted Clough-Penzien bilateral EPSD model in Eq. 3 [i.e., $S_{\ddot{g_{ip}}}(t, \beta)$], which combines the impact of both frequency non-stationarity and intensity non-stationarity. Eq. 6 displays the analytical expression of $S_{\ddot{g_{ip}}}(t, \beta)$ [90]:

$$S_{\ddot{g_{ip}}}(t, \beta) = A^2_{amp}(t) \cdot S_{amp}(t) \cdot \frac{\beta_g^4(t) + 4\xi_g^2(t)\beta_g^2(t)\beta^2}{\Big[\beta^2 - \beta_g^2(t)\Big]^2 + 4\xi_g^2(t)\beta_g^2(t)\beta^2} \cdot \frac{\beta^4}{\Big[\beta^2 - \beta_f^2(t)\Big]^2 + 4\xi_f^2(t)\beta_f^2(t)\beta^2} \tag{6}$$

in which the frequency non-stationarity of $S_{\ddot{g_{ip}}}(t, \beta)$ is reflected by $\beta_g(t)$, $\beta_f(t)$, $\xi_g(t)$ and $\xi_f(t)$, respectively, as displayed in Eq. 7. The intensity non-stationarity of $S_{\ddot{g_{ip}}}(t, \beta)$ is reflected by $A_{amp}(t)$ and $S_{amp}(t)$, in which $A_{amp}(t)$ and $S_{amp}(t)$ denote the amplitude adjustment function and spectral amplitude coefficient, with the recommended forms in Eqs. 8 and 9, respectively.

$$\beta_g(t) = \beta_0 - \mu_1 \frac{t}{T},\quad \beta_f(t) = 0.1\beta_g(t),\quad \xi_g(t) = \xi_0 + \mu_2 \frac{t}{T},\quad \xi_f(t) = \xi_g(t) \tag{7}$$

$$A_{amp}(t) = \left[\frac{t}{\mu_3} \cdot exp(1 - \frac{t}{\mu_3})\right]^{\mu_4} \tag{8}$$

$$S_{amp}(t) = \frac{\bar{a}_{\max}^2}{\gamma^2 \pi \beta_g(t) \cdot \left[2\xi_g(t) + 1/(2\xi_g(t))\right]} \tag{9}$$

in which $\mu_1$ denotes the field classification coefficient, $\mu_2$ denotes the seismic group coefficient, $\mu_3$ denotes the average peak acceleration arrival coefficient, and $\mu_4$ denotes the shape control coefficient. $\beta_0$ denotes the primary angular frequency coefficient, and $\xi_0$ denotes the soil damping coefficient. $\bar{a}_{\max}$ denotes the average peak ground acceleration, $\gamma$ denotes the equivalent peak coefficient, and $T$ denotes stochastic earthquake duration. These coefficients are all affected by the site types and design groups of the analyzing object [91]. Moreover, an iteration and modification equation is also introduced to improve the accuracy of the generated non-stationary stochastic earthquake with the target spectral requirements, as displayed in Eq. 10.

$$S_{g\ddot{i}_p}(t,\beta)|_{i+1} = \begin{cases} S_{g\ddot{i}_p}(t,\beta), & 0 < \beta \le \beta_c \\ S_{g\ddot{i}_p}(t,\beta)|_i \cdot \frac{S_a^{Tar}(\beta,\xi)^2}{S_a^{Ave}(\beta,\xi)^2|_i}, & \beta > \beta_c \end{cases} \tag{10}$$

in which $S_{g\ddot{i}_p}(t,\beta)|_{i+1}$ and $S_{g\ddot{i}_p}(t,\beta)|_i$ indicate the $(i+1)$th EPSD function and $i$th EPSD function after iteration. $S_a^{Tar}(\beta,\xi)$ indicates the target spectral acceleration, and $S_a^{Ave}(\beta,\xi)|_i$ indicates the $i$th average spectral acceleration of generated stochastic earthquakes after iteration. $\beta_c$ represents the truncated frequency, $\xi$ represents the damping ratio, and $T_0$ represents the natural structural period ($T_0 = 2\pi/\beta$).

## 4. KDE-based non-parametric cloud approach for efficient seismic fragility

Seismic fragility assessment reflects the exceeding probability of structures under earthquake excitation for a specific limit state, and it depicts the uncertain performance of structures between the demand and capacity from a probabilistic perspective. Commonly, the seismic fragility is expressed as Eq. 11:

$$P(D > C|IM) = F(a, \omega_c) = P(\Omega > \omega_c | IM = a) \tag{11}$$

in which $P$ represents the exceeding probability, $D$ represents the structural demand, and $C$ represents the structural capacity. $F$ represents the fragility function, and it is the dependent variable of intensity measure ($a$) and median structural capacity ($\omega_c$). $\Omega$ is the representation of the specific structural demand (e.g., maximum inter-story drift, maximum inter-story force, energy coefficient), as indicated in Eq. 12, and it is the extreme value [i.e., $V_{extreme}(\cdot)$] of $\boldsymbol{G}(\boldsymbol{\Delta}, t)$ in Eq. 2. The extreme value is generally adopted as the maximum or minimum result of the concerned physical object.

$$\Omega = V_{extreme}(\boldsymbol{G}(\boldsymbol{\Delta}, t)), \quad t \in [0, T] \tag{12}$$

Thus, the seismic fragility reflects the probability of demand variable $\Omega$ to exceed the capacity variable $\omega_c$ when the intensity measure is determined in the $a$-level. Eq. 11 can be reformulated into Eq. 13 after introducing a conditional PDF of $\Omega$ and a conditional probability conversion formula [i.e., $f_\Omega(\omega|IM = a)$]:

$$\begin{aligned} P(\Omega > \omega_c | IM = a) &= \int_{\omega_c}^{+\infty} f_\Omega(\omega|IM = a) d\omega \\ &= \int_{\omega_c}^{+\infty} \frac{f_{\Omega,IM}(\omega, a)}{f_{IM}(a)} d\omega = \frac{\int_{\omega_c}^{+\infty} f_{\Omega,IM}(\omega, a) d\omega}{f_{IM}(a)} \end{aligned} \tag{13}$$

in which $f_{\Omega,IM}(\omega, a)$ denotes the joint PDF between the structural demand $\Omega$ and intensity measure $IM$. $f_{IM}(a)$ denotes the marginal PDF of intensity measure $IM$. The seismic fragility can be given via a integration after the $f_{\Omega,IM}(\omega, a)$ and $f_{IM}(a)$ are calculated. More references related to this can be available from Mai et al. [92]. Then, the KDE-based approach is introduced, and for a univariate $\Theta$, the corresponding KDE-based PDF can be written as Eq. 14:

$$f_\Theta(\theta) = \frac{1}{M\lambda} \cdot \sum_{i=1}^{M} K(\frac{\theta - \theta_i}{\lambda}) \tag{14}$$

in which $K(\cdot)$ represents the kernel-based function, and the classic kernel-based function contains a series of forms (e.g., normal form, triangular form, and uniform form). In this research, a Gaussian-based kernel function is selected due to its explicit expression and broad applicability. Besides, researches indicate that when the sample sets are large enough, the kernel type shows little impact in the estimation accuracy [92]. $M$ represents the sample number, $\theta_i$ represents the individual sample of concerned variable $\Theta$, and $\lambda$ represents the indicator of bandwidth. Then, Eq. 14 can be further rewritten as Eq. 15 after introducing the standard Gaussian-based kernel function:

$$f_\Theta(\theta) = \frac{1}{M\lambda} \cdot \sum_{i=1}^{M} \frac{1}{(2\pi)^{1/2}} \cdot exp\left[-\frac{1}{2}(\frac{\theta - \theta_i}{\lambda})^2\right] \tag{15}$$

The determination of bandwidth $\lambda$ is important as the bandwidth directly affects the smoothness of PDF curves. The bandwidth $\lambda$ is commonly recommended to be $1.059\sigma \cdot M^{-0.2}$ [93], in which $\sigma$ represents the standard deviation of concerned variable $\Theta$. Eq. 16 displays the multivariate-based KDE in a $d$-dimensional scale ($\boldsymbol{\Theta} \in R^d$):

$$f_{\boldsymbol{\Theta}}(\boldsymbol{\theta}) = \frac{1}{M|\boldsymbol{\Lambda}|^{1/2}} \cdot \sum_{i=1}^{M} K\left(\boldsymbol{\Lambda}^{-1/2}(\boldsymbol{\theta} - \boldsymbol{\theta_i})\right) \tag{16}$$

in which $\boldsymbol{\Theta}$ denotes a multivariate condition. $\boldsymbol{\Lambda}$ denotes a symmetric bandwidth matrix, and its definite determinant is calculated to be $|\boldsymbol{\Lambda}|$. Eq. 17 displays the expression of joint PDF when a standard Gaussian-based kernel function is adopted for a multivariate condition:

$$f_{\boldsymbol{\Theta}}(\boldsymbol{\theta}) = \frac{1}{M|\boldsymbol{\Lambda}|^{1/2}} \cdot \sum_{i=1}^{M} \frac{1}{(2\pi)^{d/2}} \cdot exp\left[-\frac{1}{2}(\boldsymbol{\theta} - \boldsymbol{\theta_i})^T \boldsymbol{\Lambda}^{-1}(\boldsymbol{\theta} - \boldsymbol{\theta_i})\right] \tag{17}$$

in which $\boldsymbol{\theta_i}$ reflects the individual sample of concerned variable $\boldsymbol{\Theta} \in R^d$. The multivariate bandwidth matrix $\boldsymbol{\Lambda}$ is a critical link for the accuracy of joint PDF and is recommended to use the cross-validation estimators or plug-in estimators in calculation [94]. Then, in light of the aforementioned theories, the marginal PDF of $IM$ [i.e., $f_{IM}(a)$] can be obtained via Eq. 15 [according to the univariate sets of $IM$ for all the non-stationary stochastic earthquake input (i.e., $IM_i, i = 1, 2, ..., M$) ], and the joint PDF between $\Omega$ and $IM$ [i.e., $f_{\Omega,IM}(\omega, a)$] can be obtained via Eq. 17 {according to bivariate sets between $\Omega$ and $IM$ for all the non-stationary stochastic earthquake input and generated cloud points [i.e., $(\Omega_i, IM_i), i = 1, 2, ..., M$]}. Eq. 18 displays the complete analytical form of non-parametric Gaussian-kernel-based cloud-KDE for fragility assessment, in which $\lambda_{IM}$ and $\boldsymbol{\Lambda}_{\Omega,IM}$ reflect the univariate bandwidth coefficient of $IM$ as well as the bivariate bandwidth matrix between $\Omega$ and $IM$, respectively [95].

$$P(D > C|IM) = F(a, \omega_c) = \frac{\lambda_{IM}}{(2\pi|\boldsymbol{\Lambda}_{\Omega,IM}|)^{1/2}} \cdot \frac{\displaystyle\int_{\omega_c}^{+\infty} \sum_{i=1}^{M} exp\left[-\frac{1}{2}(\begin{matrix} a - IM_i \\ \omega - \Omega_i \end{matrix})^T \cdot \boldsymbol{\Lambda}_{\Omega,IM}^{-1} \cdot (\begin{matrix} a - IM_i \\ \omega - \Omega_i \end{matrix})\right] d\omega}{\displaystyle\sum_{i=1}^{M} exp\left[-\frac{1}{2}(\frac{a - IM_i}{\lambda_{IM}})^2\right]} \tag{18}$$

## 5. Application example

In light of the aforementioned framework, this section presents the application of the KDE-based non-parametric cloud approach for efficient seismic fragility estimation under non-stationary excitation via a three-span-six-story RCF. The building information, modelling approach, generated non-stationary stochastic excitation, and cloud-KDE result discussions are included. More details are illustrated as follows.

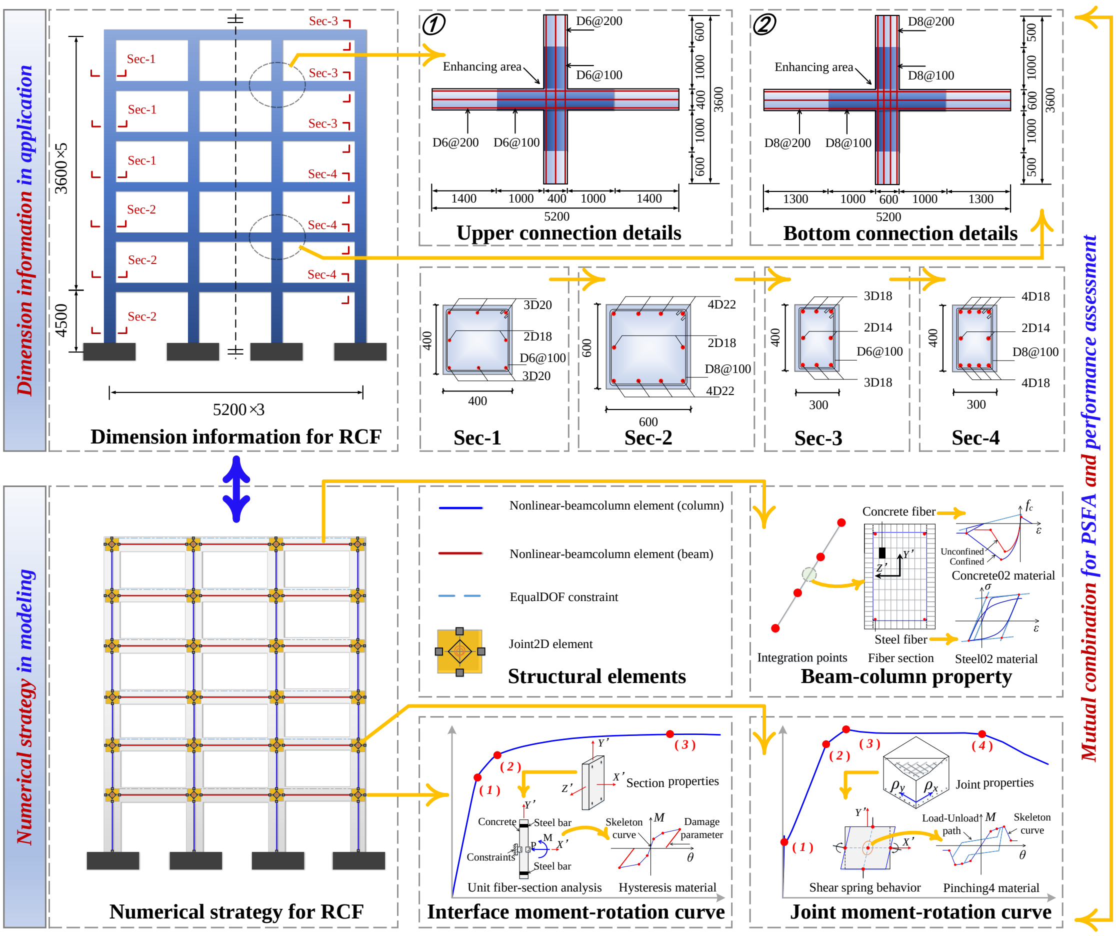


Figure 2: The dimension information in application and numerical strategy in modelling

### 5.1. Building information

The building information of the application example is shown in Fig. 2. The design span length is 5200 m with a total span number of 3. The design story height is 4500 m for bottom story and 3600 m for other stories, with a total story number of 6. From the bottom to the third story, the cross section of column (i.e., Sec-2) is 600 mm×600 mm, with four D22 reinforcements on both top sides and bottom sides. The cross section of beam (i.e., Sec-4) is 300 mm×400 mm, with four D18 reinforcements on both top sides and bottom sides. From the fourth story to the sixth story, the cross section of column (i.e., Sec-1) is 400 mm×400 mm, with three D20 reinforcements on both top sides and bottom sides. The cross section of beam (i.e., Sec-3) is 300 mm×400 mm, with three D18 reinforcements on both top sides and bottom sides. For the bottom connection (storey 1-3), the stirrups are adopted as D8, and for the top connection (storey 4-6), the stirrups are adopted as D6. The enhanced zones of stirrups (with an interval of 100 mm) are from the column surface to an extending distance of 1000 mm. The design grade of concrete is C30 with the standard cubic compressive strength of 30 MPa, the design grade of reinforcing steel is HRB335 with the standard tensile strength of 335 MPa, and the design grade of constructional stirrup is HPB300 with the standard tensile strength of 300 MPa. Worth mentioning is that the standard value herein represents a 95% guaranteeing rate and is not the same as the median value (i.e., 50% guaranteeing rate). The detailed random variables and statistical parameters in the application example are listed in Tab. 1.

Table 1: The random variables and statistical parameters in the application example

| Random variables | Symbol | Distribution | Mean (unit) | COV | Reference |
|---|---|---|---|---|---|
| Earthquake phase angle1 | $P_1$ | Uniform | 3.142 (1) | 0.577 | [96] |
| Earthquake phase angle2 | $P_2$ | Uniform | 3.142 (1) | 0.577 | [96] |
| Concrete bulk density | $\gamma$ | Normal | 26.5 ($kN/m^3$) | 0.0698 | [97] |
| Span length | $sb$ | Normal | 5200 ($mm$) | 0.003 | [98] |
| Bottom story height | $hf$ | Normal | 4500 ($mm$) | 0.003 | [98] |
| Standard story height | $ha$ | Normal | 3600 ($mm$) | 0.003 | [98] |
| Damping ratio | $\varsigma$ | Normal | 0.05 (1) | 0.1 | [99] |
| Core concrete compressive strength | $f_{cp,core}$ | Lognormal | 33.6 ($MPa$) | 0.21 | [99] |
| Core concrete peak strain | $\varepsilon_{cp,core}$ | Lognormal | 0.0022 (1) | 0.17 | [99] |
| Rebar yielding strength | $f_y$ | Lognormal | 378 ($MPa$) | 0.07 | [99] |
| Rebar elastic modulus | $E$ | Lognormal | 201000 ($MPa$) | 0.033 | [100] |

### 5.2. Modelling approach

The modelling approach of the application example is also presented in Fig. 2. In this analysis, the OpenSees software is selected [101], which is a widely-used procedure for the earthquake engineering and structural assessment. In this modelling, the structural beams and columns are characterized by the nonlinear-beam-column element [102], which is a force-based nonlinear element and is generated through the flexibility method. The static equilibrium condition of this element is stable even under the strong non-linearity environment, and even small number of elements can effectively capture the structural behaviors. At each integration point of nonlinear-beam-column element, the fiber sections (i.e., steel fiber of Steel02 and concrete fiber of Concrete02) are assigned to characterize the mechanical properties [103, 104]. The influence of stirrups is well considered via the confined concrete model [105]. As the beam-column joint is the key section of frames, the Joint2D element is well used in this modelling, which is featured with one center spring and four interfacial springs. The center spring reflects the shear damage of core zones, and it is assigned with the Pinching4 material, whose parameters can be acquired via the modified compression field theory (i.e., joint moment-rotation relationship) [106]. The interfacial spring reflects the bond-slip effects of reinforcement, and it is assigned with the Hysteresis material, whose parameters can be acquired via the zero-length fiber-section analysis (i.e., interfacial moment-rotation relationship) [107, 108]. Both the Pinching4 and Hysteretic materials contain the coefficients to quantify the degradation, damage or pinching properties. Besides, the equalDOF is applied to each story (i.e., outer two nodes) to constrain the horizontal deformation and to conform to the rigid-floor assumption [109].

### 5.3. Generated non-stationary stochastic excitation

In this analysis, the site type is chosen to be type-III, followed with an equivalent shear velocity between 150 to 250 m/s. The seismic group is chosen to be type-I in consistent with the requirements in the Chinese seismic code [110]. The fortification intensity is 8 degrees (PGA=0.2 g) with a maximum exceeding probability of 10 % in fifty design years. Based on the procedure in Sec. 3, the Gaussian-oriented non-stationary stochastic excitations for structural response assessment are generated, and two independent stochastic phase angle variables in Eq. 5 (i.e., $P_1$ and $P_2$) are involved, as listed in Tab. 1. $P_1$ and $P_2$ are sampled by LHS for each intensity bandwidth to generate the non-stationary stochastic excitation and to form the stochastic cloud points of structural response. The corresponding parameter values of non-stationary stochastic excitations adopted in this analysis can be found in Tab. 2. Fig. 3(a) presents the bilateral evolutionary power spectral density function, Fig. 3(b) presents the average acceleration with target (cloud points=1600), Fig. 3(c) presents the standard deviation with target (cloud points=1600), and Fig. 3(d) presents the typical non-stationary stochastic earthquake for the fortification intensity. Worth mentioning is that in the cloud analysis of this paper, the average peak ground acceleration $\bar{a}_{\max}$ varies for different intensity bandwidth, and herein the fortification intensity is adopted as a demonstration.

Table 2: The coefficient values in the non-stationary stochastic earthquake input

| Coefficients | $\mu_1$ $(s^{-1})$ | $\mu_2$ (1) | $\mu_3$ (s) | $\mu_4$ (1) | T (s) | $\beta_0$ $(s^{-1})$ | $\xi_0$ (1) | $\gamma$ (1) | $\bar{a}_{\max}$ $(m \cdot s^{-2})$ | $\beta_{if}$ $(rad \cdot s^{-1})$ | $\beta_c$ $(rad \cdot s^{-1})$ | $N_{tr}$ (1) |
|---|---|---|---|---|---|---|---|---|---|---|---|---|
| Values | 5.0 | 0.2 | 6.0 | 2.0 | 25.0 | 16.0 | 0.6 | 2.85 | 1.96 | 0.20 | 1.57 | 1500 |

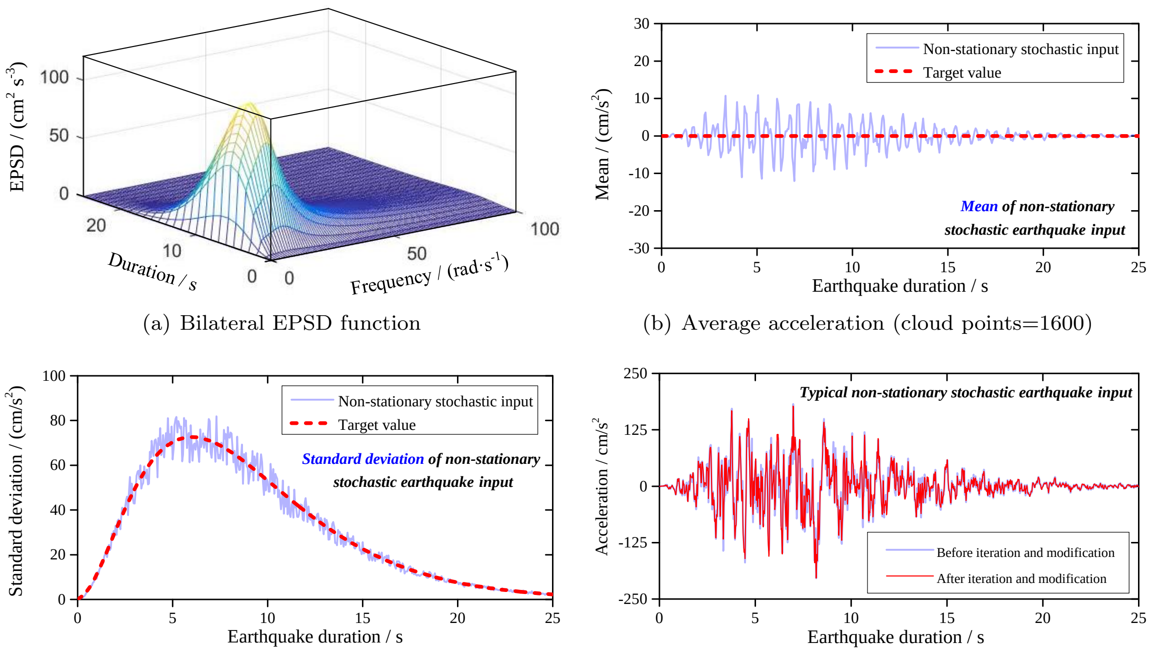


(a) Bilateral EPSD function

(b) Average acceleration (cloud points=1600)

(c) Standard deviation (cloud points=1600)

(d) Non-stationary excitation (fortification level)

Figure 3: Non-stationary stochastic earthquake excitation

### 5.4. Cloud-KDE result discussions

In this analysis, the classic cloud-LR approach and cloud-MCS approach are also incorporated for comparison with the cloud-KDE approach. The cloud-LR approach is the most-commonly adopted parametric strategy for seismic fragility in light of the lognormal assumption, and its analytical expression is given in

Eq. 1. The cloud-MCS approach is a non-parametric approach which requires mass statistical data, and it is commonly used as a benchmark for validation of unknown variable. As for the cloud-KDE approach, its procedure is illustrated in Sec. 4 and Eq. 18.

During the research process, the random samples of variables are generated via the LHS, which is an efficient stratified sampling technique. As indicated in Fig. 1, the earthquake number for each intensity bandwidth and the total cloud points are needed to be determined in advance for the cloud-KDE approach of seismic fragility. In this study, the intensity measure is adopted as the peak ground acceleration (PGA), and totally 40 intensity bandwidths are considered (i.e., from 0.1g to 4.0g with an interval of 0.1g). Worth noticing herein is that the intensity bandwidth corresponds to the $\bar{a}_{\max}$ in Eq. 9, and the actual PGA of the generated earthquake is stochastic due to the representation of stochastic functions (e.g., the intensity bandwidth is set as 0.1g, while the PGA of the generated non-stationary stochastic earthquake at this level may be 0.09g or 0.11g). This is also the principle to realize the stochastic cloud points of structural response in this analysis [111]. The engineering demand parameter is adopted as the maximum inter-story drift ratio (MIDR) in this analysis. The MIDR is the most-widely accepted index for performance assessment of building structures, and it is calculated by the deterministic nonlinear time-history analysis using the numerical model. Then, totally six groups of stochastic cloud points are considered, i.e., (1) 1 earthquake for each bandwidth and total 40 cloud points; (2) 3 earthquakes for each bandwidth and total 120 cloud points; (3) 5 earthquakes for each bandwidth and total 200 cloud points; (4) 10 earthquakes for each bandwidth and total 400 cloud points; (5) 20 earthquakes for each bandwidth and total 800 cloud points; and (6) 40 earthquakes for each bandwidth and total 1600 cloud points. Besides, four limit states are defined for seismic fragility assessment in this analysis, i.e., limit state 1 with the MIDR of 1% (LS1), limit state 2 with the MIDR of 2% (LS2), limit state 3 with the MIDR of 4% (LS3), and limit state 4 with the MIDR of 6% (LS4). Herein the MIDR of each limit state corresponds to the median value of structural capacity [112, 113, 114].

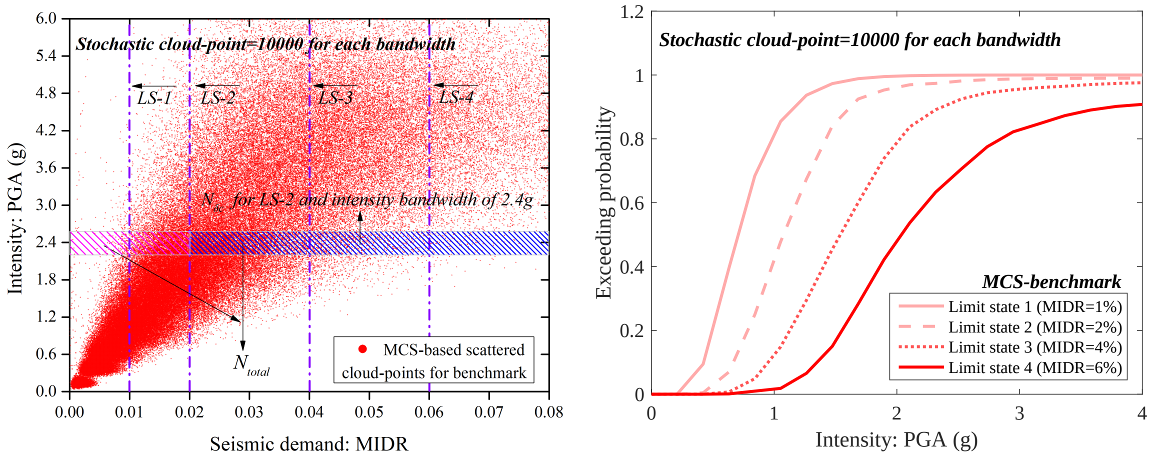


(a) Scattered point samples in cloud-MCS approach

(b) Seismic fragility curves in cloud-MCS approach

Figure 4: Scattered point samples and seismic fragility curves in cloud-MCS approach

Fig. 4 presents the scattered point samples and seismic fragility curves in cloud-MCS approach, and during the procedure, 10000 scattered samples are stochastically generated and calculated for each intensity bandwidth (i.e., from 0.1g to 4.0g with an interval of 0.1g). Fig. 5 presents the stochastic cloud points in logarithmic coordinate system for six groups (i.e., number of 40, 120, 200, 400, 800 and 1600), and linear regressions via the least-squares method are also obtained for the parametric cloud-LR approach. The corresponding regression coefficients and logarithmic variances are also displayed [e.g., in Fig. 5(a), ln(MIDR)=1.0929×ln(PGA)-3.646 with the logarithmic demand variance of 0.2259 when the stochastic cloud-point=40]. The logarithmic standard deviation of capacity is assumed to vary from 0.2 to 0.47 [115].

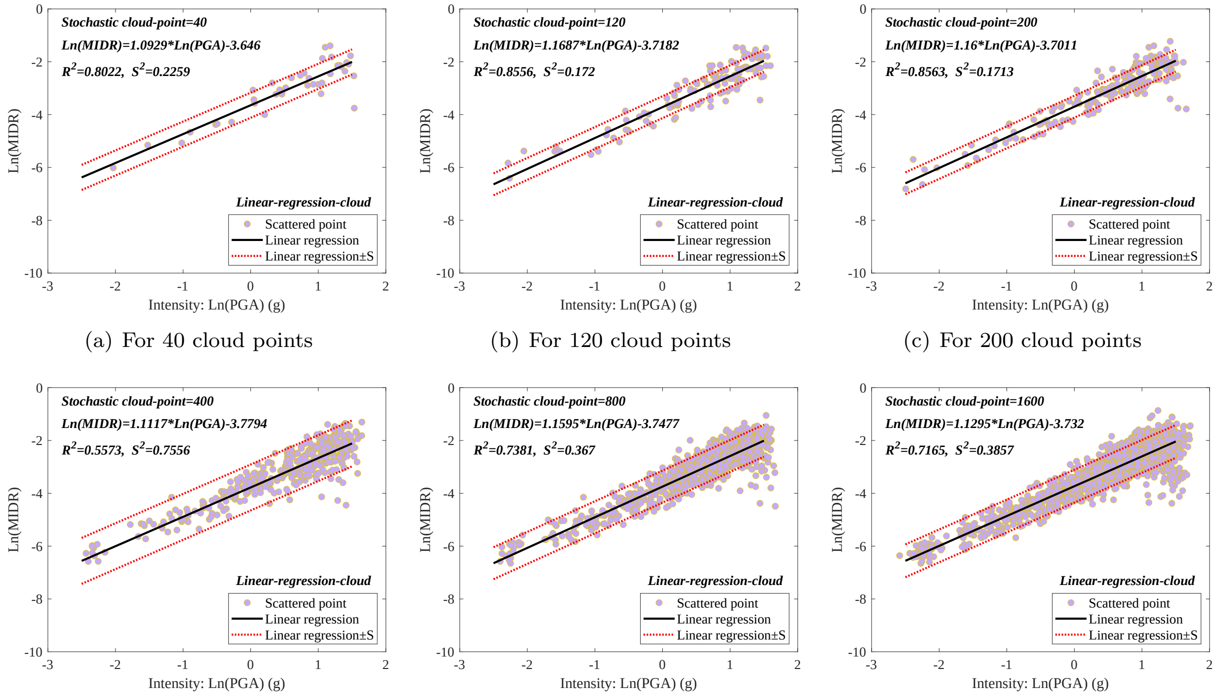


(a) For 40 cloud points (b) For 120 cloud points (c) For 200 cloud points

(d) For 400 cloud points (e) For 800 cloud points (f) For 1600 cloud points

Figure 5: Linear regressions and cloud points in cloud-LR approach

Then, these parameters are taken into Eq. 1 to derive the lognormal-based parametric seismic fragility curves. Figs. 6 to 9 present the detailed procedure of cloud-KDE approach for all the six groups. Fig. 6 displays the marginal PDF (blue line) and marginal CDF (pink line) of intensity measure via the one-dimensional Gaussian cloud-KDE approach, as indicated in Eq. 15. The Gaussian kernels and histograms are also given for illustration. It can be found that with the increase of cloud points, the platform section of marginal PDF is more stable. In Fig. 6(f), the marginal PDF is almost formed by the envelops of histograms, although there exists small fluctuation near the PGA of 0 (i.e., intensity samples can be infinitely close to 0 but larger than 0). Fig. 7 displays the joint-PDF between engineering demand parameter (i.e., MIDR in this analysis) and intensity measure (i.e., PGA in this analysis) via the two-dimensional Gaussian cloud-KDE approach. It can be found that with the increase of cloud points, the joint PDF gradually changes from the flat condition to sharp condition, with the maximum joint value of 4 for 40 cloud points to the maximum joint value of 14 for 1600 cloud points. As mentioned in Sec. 2, the optimal one-dimensional bandwidth for PGA (i.e., $\lambda_{IM}$) and optimal two-dimensional bandwidth between MIDR and PGA (i.e., $\mathbf{\Lambda}_{\Omega,IM}$) are important for the smoothness of PDF and accuracy of fragility results. The one-dimensional bandwidth is calculated via the recommended equation in Sec. 4, and the two-dimensional bandwidth is calculated via the plug-in estimators in R procedure in Sec. 4 [94]. Tab 3 summarizes the detailed bandwidth values of both one-dimensional and two-dimensional conditions for all the six groups. Fig. 8 presents the joint-PDF under certain MIDR (i.e., MIDR=0.01, 0.02, 0.03, 0.04, 0.05 and 0.06), and Fig. 9 presents the joint-PDF under certain PGA (i.e., PGA=0.1g, 0.2g, 0.3g, 0.4g, 0.6g and 0.8g). In general, the joint-PDF under MIDR moves towards right and becomes more flattened with the increase of MIDR, and fluctuation phenomenon appears in PDF value when the PGA approximates to a large level. Similarly, the joint-PDF under PGA also moves towards right with the increase of PGA, but the corresponding curve shape is relatively stable.

Figs. 10 and 11 present the fragility comparison of the cloud-MCS, cloud-LR and cloud-KDE approaches. The results of cloud-MCS are depicted in red, the results of cloud-KDE are depicted in blue, and the results of cloud-LR are depicted in black, respectively. All the four limit states and six cloud groups are incorporated.

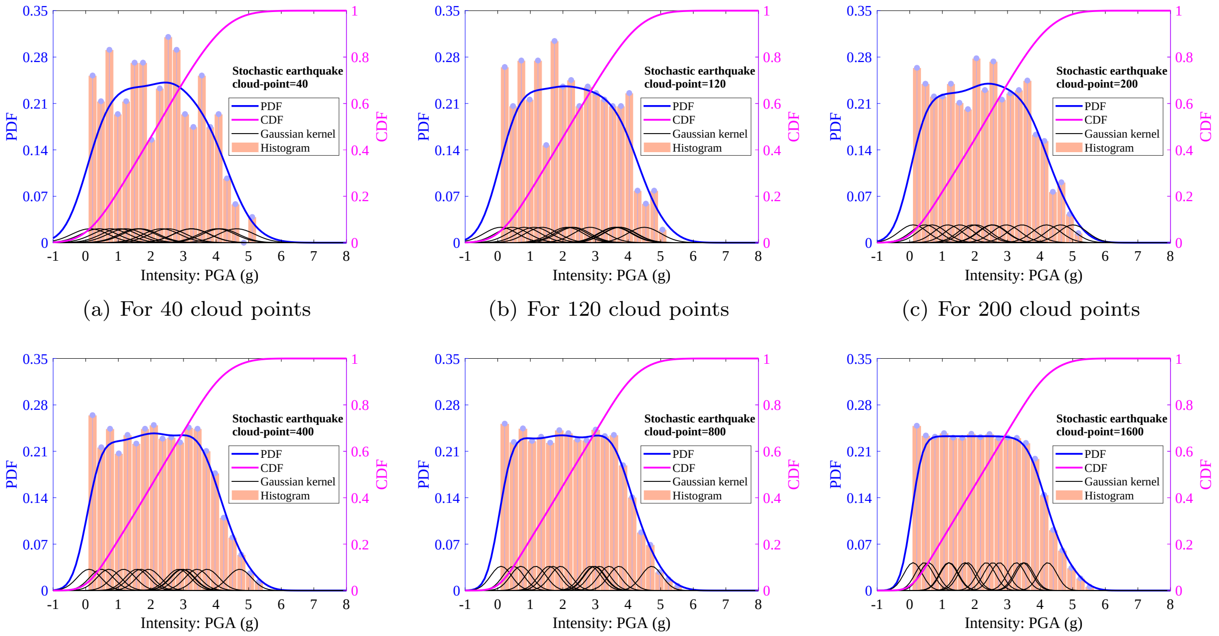


(a) For 40 cloud points (b) For 120 cloud points (c) For 200 cloud points

(d) For 400 cloud points (e) For 800 cloud points (f) For 1600 cloud points

Figure 6: Marginal PDF and CDF of IM via the one-dimensional Gaussian cloud-KDE approach

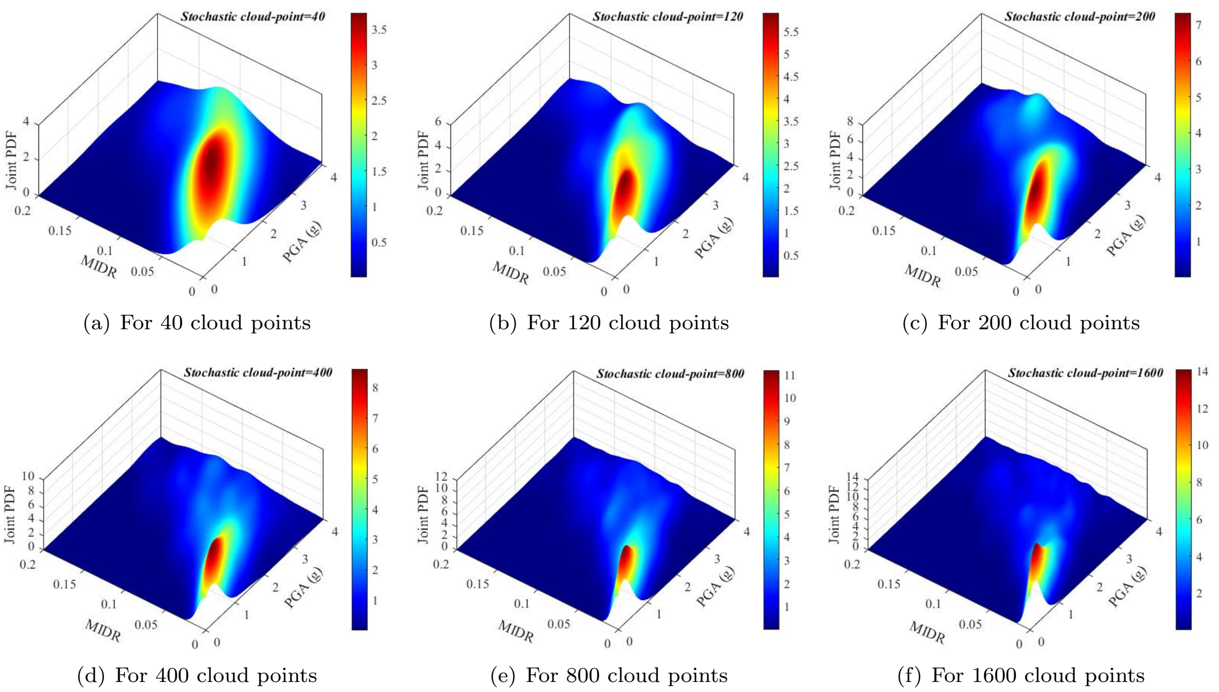


(a) For 40 cloud points (b) For 120 cloud points (c) For 200 cloud points

(d) For 400 cloud points (e) For 800 cloud points (f) For 1600 cloud points

Figure 7: Joint-PDF between EDP and IM via the two-dimensional Gaussian cloud-KDE approach

The fragility medians of all the three approaches are given, and a coefficient, namely the extent of fitting accuracy (FAE), is also derived to judge the deviation with the benchmark cloud-MCS approach. The FAE

Table 3: The detailed bandwidth values of both one-dimensional and two-dimensional conditions

| Cloud number | Optimal one-dimensional bandwidth of PGA | Optimal two-dimensional bandwidth between MIDR and PGA |
|---|---|---|
| 40 cloud points | 0.778974 | $\begin{bmatrix} 0.555846, & 0.012657 \\ 0.012657, & 0.000669 \end{bmatrix}$ |
| 120 cloud points | 0.592391 | $\begin{bmatrix} 0.236836, & 0.004959 \\ 0.004959, & 0.000251 \end{bmatrix}$ |
| 200 cloud points | 0.558141 | $\begin{bmatrix} 0.161125, & 0.003115 \\ 0.003115, & 0.000161 \end{bmatrix}$ |
| 400 cloud points | 0.504974 | $\begin{bmatrix} 0.131939, & 0.002561 \\ 0.002561, & 0.000122 \end{bmatrix}$ |
| 800 cloud points | 0.436482 | $\begin{bmatrix} 0.082247, & 0.001463 \\ 0.001463, & 0.000072 \end{bmatrix}$ |
| 1600 cloud points | 0.387087 | $\begin{bmatrix} 0.052286, & 0.000927 \\ 0.000927, & 0.000047 \end{bmatrix}$ |

is calculated by evaluating the gaps between the target approach and cloud-MCS approach, and its principle can be found in Feng et al [38]. Tab. 4 lists the fragility medians for all the three fragility approaches and six groups of cloud points, and Tab. 5 lists the FAE of KDE-MCS and LR-MCS for all the six groups of cloud points and four limit states. In general, for both the cloud-LR and cloud-KDE approaches, the obtained seismic fragility curves show similar tendency with the cloud-MCS approach, and with the increase of cloud number, the corresponding fitting extent is more closer and indicates a better effect. Take the fragility median as an instance, the benchmark values via the cloud-MCS approach are given as 0.7079g, 1.0765g, 1.5396g and 2.0378g from LS1 to LS4. Utilizing the cloud-KDE approach, the corresponding fragility medians are obtained as 0.5828g, 0.9779g, 1.4463g and 2.0715g for 40 cloud points, with the changing ratios computed as 17.67%, 9.16%, 6.06% and 1.65%, respectively. When the cloud points increase to 1600, the corresponding fragility medians are obtained as 0.6929g, 1.0637g, 1.5129g and 2.0235g, with the changing ratios computed as 2.12%, 1.19%, 1.73% and 0.70%, which are more closer to the cloud-MCS results than the condition of 40 cloud points. The phenomenon can also be found in the coefficient of FAE. For the 40 cloud points, the FAE of KDE-MCS is given as 0.0864, 0.0606, 0.0405 and 0.0336 from LS1 to LS4, and the corresponding FAE of LR-MCS is given as 0.0468, 0.0711, 0.0836 and 0.0902, respectively. When the cloud points increase to 1600, the FAE of KDE-MCS is given as 0.0144, 0.0126, 0.0131 and 0.0097, and the corresponding FAE of LR-MCS is given as 0.0321, 0.0369, 0.0302 and 0.0292, respectively. The FAE drops for both approaches and all the four limit states, with an average reducing ratio of 75.33% for cloud-KDE approach and 52.75% for cloud-LR approach, which indicates a greater fragility result with the cloud number increasing.

At the same time, the non-parametric cloud-KDE approach presents a comparable fragility with the benchmark cloud-MCS approach, and in most conditions, the cloud-KDE approach even shows less deviation in comparison with the classic parametric cloud-LR approach. Take the fragility median under the LS4 as an instance, the deviation ratios between the cloud-KDE and cloud-MCS approaches are calculated as 1.65% (cloud number=40), 4.73% (cloud number=120), 0.90% (cloud number=200), 2.70% (cloud number=400), 0.43% (cloud number=800) and 0.70% (cloud number=1600), respectively. Correspondingly, the deviation ratios between the cloud-LR and cloud-MCS approaches are calculated as 10.67% (cloud number=40), 9.84% (cloud number=120), 9.76% (cloud number=200), 5.49% (cloud number=400), 6.43% (cloud number=800) and 5.12% (cloud number=1600), respectively. It can be observed that for all the cloud number conditions, the median deviations of cloud-KDE approach are smaller than the cloud-LR approach with the dropping ratios of 84.50%, 51.94%, 90.80%, 50.72%, 93.36% and 86.30%, respectively, which demonstrates a more reliable result of cloud-KDE approach in a sense. The same conclusions can be achieved from the FAE under the LS4. The FAE of KDE-MCS is computed as 0.0336 (cloud number=40), 0.0392 (cloud number=120), 0.0254 (cloud number=200), 0.0201 (cloud number=400), 0.0118 (cloud number=800) and 0.0097 (cloud number=1600), while the FAE of LR-MCS is computed as 0.0902 (cloud number=40), 0.0813 (cloud number=120), 0.0560 (cloud number=200), 0.0431 (cloud number=400), 0.0345 (cloud number=800) and 0.0292 (cloud number=1600), respectively. For each cloud number condition, the average FAE of KDE-MCS is smaller than the LR-MCS, with the dropping ratios of 62.75%, 51.78%, 54.64%, 53.36%, 65.80% and 66.78% (average of 59.19%), respectively. Similar findings can be acquired for LS1 (average of 31.05%), LS2 (average of 37.40%) and LS3 (average of 51.96%). The analysis verifies the effectiveness of the non-parametric cloud-KDE approach without requiring more computation work (i.e., same as the parametric cloud-LR approach and much less than the benchmark cloud-MCS approach), and meanwhile it indicates a comparable accuracy with the classic fragility approaches (i.e., less deviation than the parametric cloud-LR approach and much closer to the benchmark cloud-MCS approach).

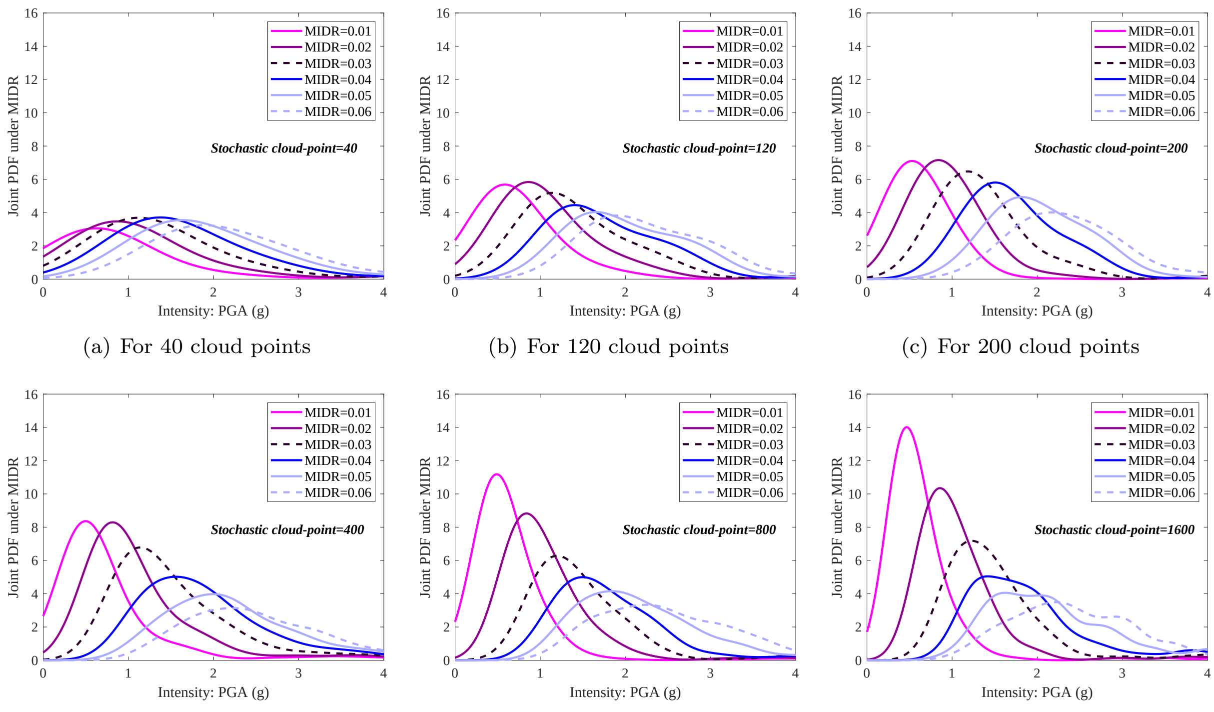


(a) For 40 cloud points (b) For 120 cloud points (c) For 200 cloud points

(d) For 400 cloud points (e) For 800 cloud points (f) For 1600 cloud points

Figure 8: Development of joint-PDF along with PGA under certain MIDR

## 6. Parametric analysis of the critical factors

In this section, the parametric analysis is further performed for the non-parametric cloud-KDE approach [116, 117, 118], and two critical factors that potentially influence the assessment result are elaborately discussed (i.e., the intensity measure and bandwidth). First, the intensity measure is changed to the spectral acceleration of the fundamental period [$S_a(T_1)$], and the seismic fragility is given via the non-parametric cloud-KDE approach for all the six groups of stochastic cloud points as well as the four limit states, as implemented in Sec. 5. Then, the parametric analysis of both the one-dimensional bandwidth and two-dimensional bandwidth is conducted, as the determination of bandwidth is an important step in the non-parametric cloud-KDE approach for fragility. Fig. 12 presents the parametric analysis of intensity measure, in which the green lines are obtained via $S_a(T_1)$ through the non-parametric cloud-KDE approach, and red lines are obtained via $S_a(T_1)$ through the benchmark cloud-MCS approach. The corresponding medians and

Table 4: The fragility medians for all the three fragility approaches and six groups of cloud points

| Type and number | LS1 (g) | LS2 (g) | LS3 (g) | LS4 (g) |
|---|---|---|---|---|
| MCS-cloud (via PGA) | 0.7079 | 1.0765 | 1.5396 | 2.0378 |
| MCS-cloud [via $S_a(T_1)$] | 0.7539 | 1.1520 | 1.6416 | 2.1397 |
| KDE-cloud for 40 points (via PGA) | 0.5828 | 0.9779 | 1.4463 | 2.0715 |
| KDE-cloud for 120 points (via PGA) | 0.5743 | 0.9831 | 1.5298 | 2.1342 |
| KDE-cloud for 200 points (via PGA) | 0.6546 | 1.0431 | 1.4693 | 2.0195 |
| KDE-cloud for 400 points (via PGA) | 0.6810 | 1.0776 | 1.5303 | 2.0929 |
| KDE-cloud for 800 points (via PGA) | 0.6867 | 1.0693 | 1.5009 | 2.0465 |
| KDE-cloud for 1600 points (via PGA) | 0.6929 | 1.0637 | 1.5129 | 2.0235 |
| LR-cloud for 40 points (via PGA) | 0.6998 | 1.0756 | 1.5750 | 2.2552 |
| LR-cloud for 120 points (via PGA) | 0.7160 | 1.0883 | 1.5779 | 2.2384 |
| LR-cloud for 200 points (via PGA) | 0.7262 | 1.1238 | 1.6557 | 2.2367 |
| LR-cloud for 400 points (via PGA) | 0.6879 | 1.0454 | 1.5155 | 2.1496 |
| LR-cloud for 800 points (via PGA) | 0.6999 | 1.0604 | 1.5330 | 2.1688 |
| LR-cloud for 1600 points (via PGA) | 0.6392 | 0.9967 | 1.4782 | 2.1422 |
| KDE-cloud for 40 points [via $S_a(T_1)$] | 0.6235 | 1.0464 | 1.5475 | 2.2165 |
| KDE-cloud for 120 points [via $S_a(T_1)$] | 0.6146 | 1.0519 | 1.6369 | 2.2836 |
| KDE-cloud for 200 points [via $S_a(T_1)$] | 0.7004 | 1.1161 | 1.5722 | 2.1608 |
| KDE-cloud for 400 points [via $S_a(T_1)$] | 0.7335 | 1.1569 | 1.6393 | 2.2376 |
| KDE-cloud for 800 points [via $S_a(T_1)$] | 0.7348 | 1.1441 | 1.6059 | 2.1898 |
| KDE-cloud for 1600 points [via $S_a(T_1)$] | 0.7414 | 1.1381 | 1.6188 | 2.1652 |

Table 5: The FAE of KDE-MCS and LR-MCS for all the six groups of cloud points and four limit states

| Type and number | LS1 (1) | LS2 (1) | LS3 (1) | LS4 (1) |
|---|---|---|---|---|
| FAE of KDE-MCS for 40 points (via PGA) | 0.0864 | 0.0606 | 0.0405 | 0.0336 |
| FAE of KDE-MCS for 120 points (via PGA) | 0.0834 | 0.0551 | 0.0316 | 0.0392 |
| FAE of KDE-MCS for 200 points (via PGA) | 0.0484 | 0.0264 | 0.0276 | 0.0254 |
| FAE of KDE-MCS for 400 points (via PGA) | 0.0288 | 0.0096 | 0.0116 | 0.0201 |
| FAE of KDE-MCS for 800 points (via PGA) | 0.0143 | 0.0103 | 0.0141 | 0.0118 |
| FAE of KDE-MCS for 1600 points (via PGA) | 0.0144 | 0.0126 | 0.0131 | 0.0097 |
| FAE of LR-MCS for 40 points (via PGA) | 0.0468 | 0.0711 | 0.0836 | 0.0902 |
| FAE of LR-MCS for 120 points (via PGA) | 0.0438 | 0.0659 | 0.0760 | 0.0813 |
| FAE of LR-MCS for 200 points (via PGA) | 0.0281 | 0.0287 | 0.0481 | 0.0560 |
| FAE of LR-MCS for 400 points (via PGA) | 0.0229 | 0.0250 | 0.0261 | 0.0431 |
| FAE of LR-MCS for 800 points (via PGA) | 0.0209 | 0.0244 | 0.0266 | 0.0345 |
| FAE of LR-MCS for 1600 points (via PGA) | 0.0321 | 0.0369 | 0.0302 | 0.0292 |
| FAE of KDE-MCS for 40 points [via $S_a(T_1)$] | 0.0908 | 0.0633 | 0.0437 | 0.0330 |
| FAE of KDE-MCS for 120 points [via $S_a(T_1)$] | 0.0868 | 0.0566 | 0.0363 | 0.0439 |
| FAE of KDE-MCS for 200 points [via $S_a(T_1)$] | 0.0518 | 0.0246 | 0.0320 | 0.0211 |
| FAE of KDE-MCS for 400 points [via $S_a(T_1)$] | 0.0253 | 0.0081 | 0.0187 | 0.0328 |
| FAE of KDE-MCS for 800 points [via $S_a(T_1)$] | 0.0157 | 0.0102 | 0.0209 | 0.0188 |
| FAE of KDE-MCS for 1600 points [via $S_a(T_1)$] | 0.0131 | 0.0146 | 0.0200 | 0.0142 |

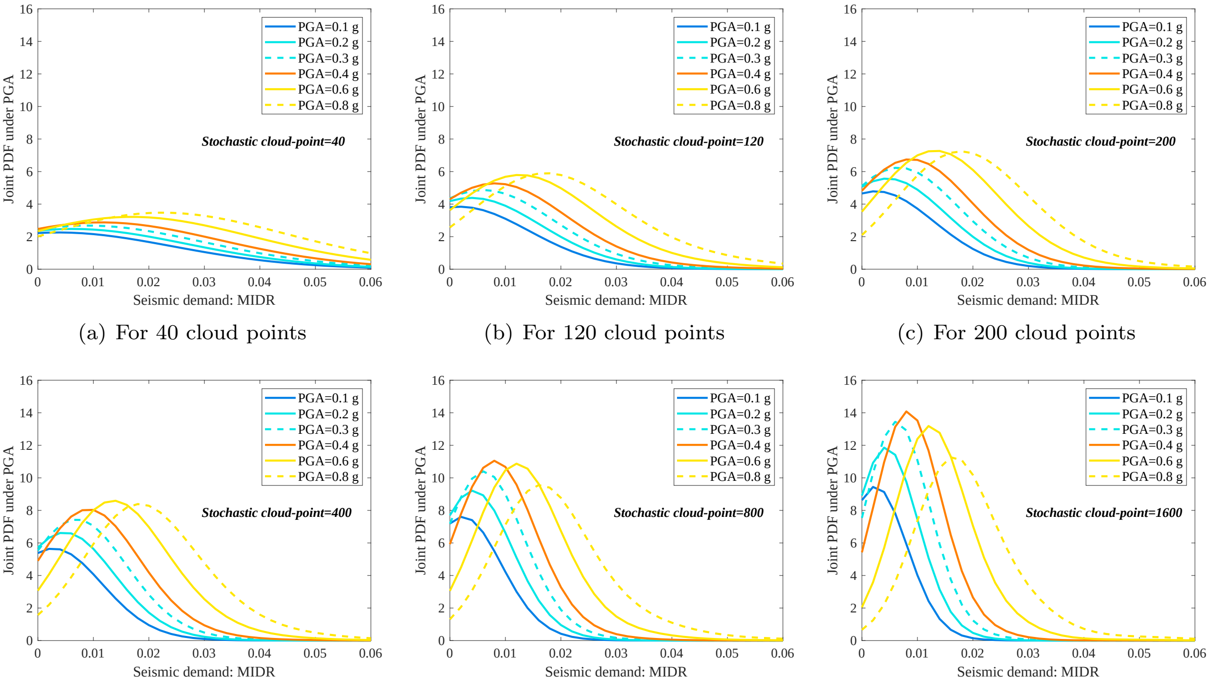


(a) For 40 cloud points (b) For 120 cloud points (c) For 200 cloud points

(d) For 400 cloud points (e) For 800 cloud points (f) For 1600 cloud points

Figure 9: Development of joint-PDF along with MIDR under certain PGA

FAE are also given in Fig. 12 and summarized in Tabs. 4 and 5. Fig. 13 presents the parametric analysis of one-dimensional bandwidth in the non-parametric cloud-KDE approach for fragility, and four scenarios are especially compared as an instance (i.e., 200 cloud points and LS2, 200 cloud points and LS4, 400 cloud points and LS2, 400 cloud points and LS4, respectively). Totally seven conditions are considered (i.e., one-dimensional bandwidth of 0.1, 0.2, 0.3, optimal value as in Sec. 5, 0.5, 0.6, and 0.7, respectively). Similarly, Fig. 14 presents the parametric analysis of two-dimensional bandwidth in the non-parametric cloud-KDE approach for four scenarios (i.e., 200 cloud points and LS2, 200 cloud points and LS4, 400 cloud points and LS2, 400 cloud points and LS4, respectively), and totally seven conditions are considered (i.e., two-dimensional optimal bandwidth multiplied by 0.1, 0.25, 0.5, 1.0 as in Sec. 5, 2.0, 4.0, and 6.0, respectively). For both Figs. 13 and 14, the MCS-based results are given with the dotted red lines, and the FAE is also calculated as indicated in the Tab. 6.

In general, it can be observed from Fig. 12 that similar tendency between the non-parametric cloud-KDE approach and benchmark cloud-MCS approach is obtained via the measure of $S_a(T_1)$, which is in agreement with the conclusion of Fig. 10 via the measure of PGA. With the increase of stochastic cloud points, the FAE indicates a smaller value, which proves a better fitting accuracy against the benchmark cloud-MCS approach. For the 40 stochastic cloud points, the FAE from LS1 to LS4 is given as 0.0908, 0.0633, 0.0437 and 0.0330, and for the 1600 stochastic cloud points, the FAE from LS1 to LS4 is dropped to 0.0131, 0.0146, 0.0200 and 0.0142, accompanied with the reducing degree of 85.57%, 76.94%, 54.23%, and 56.97%, respectively. From Figs. 10 and 12, it can also be found that the change of intensity measure shows little impact on the non-parametric cloud-KDE approach for seismic fragility, which provides some reference for the further non-parametric fragility investigation and demonstrates certain superiority than the classic parametric approach in a sense (e.g., classic parametric approach is more sensitive to the selection of intensity measure as introduced in [119, 120]).

From Figs. 13 and 14, it is found that the change of one-dimensional or two-dimensional bandwidth leads to obvious variations of the generated fragility curves, from both the perspective of fitting accuracy

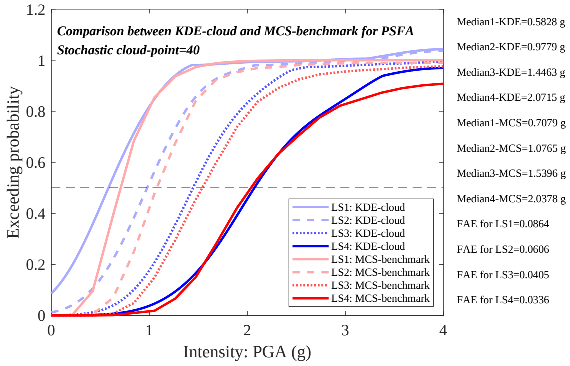


(a) For 40 cloud points

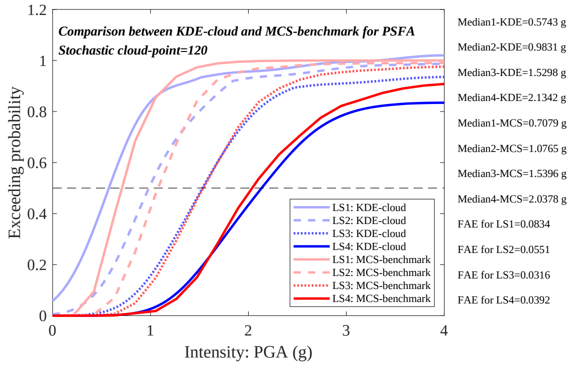


(b) For 120 cloud points

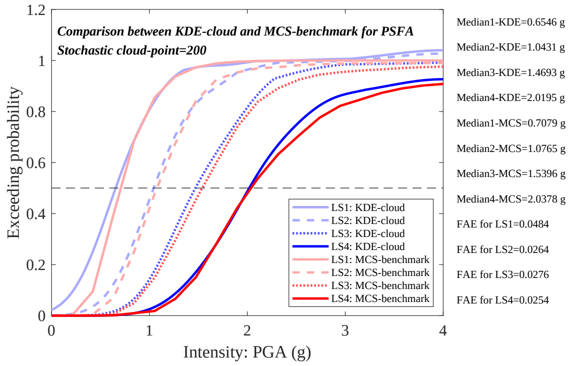


(c) For 200 cloud points

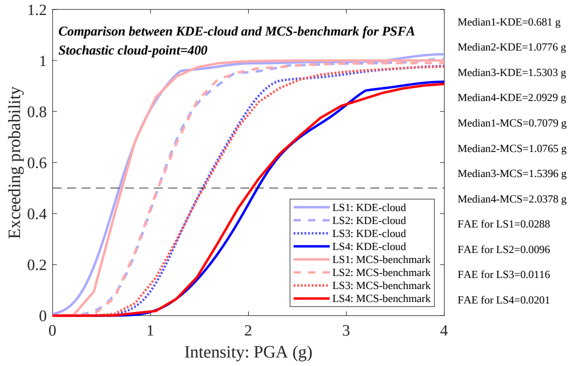


(d) For 400 cloud points

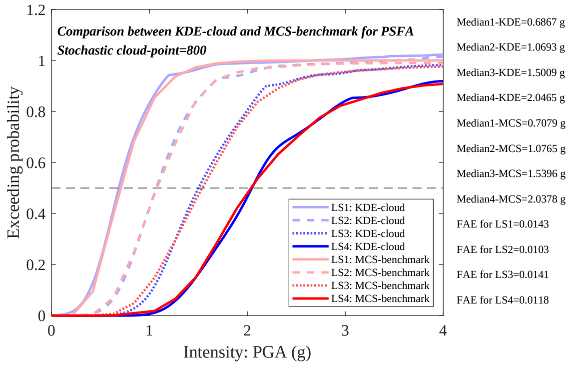


(e) For 800 cloud points

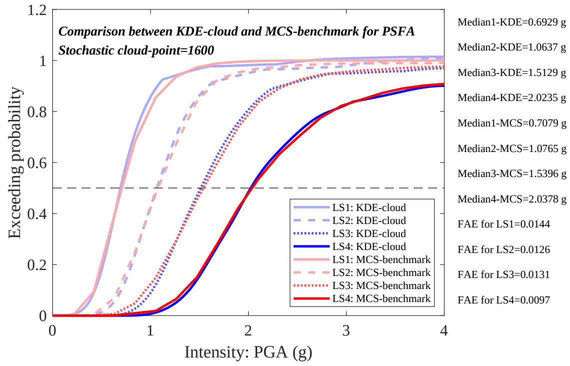


(f) For 1600 cloud points

Figure 10: Comparison between the non-parametric cloud-KDE approach and the benchmark cloud-MCS approach

and curve smoothness. This also proves that the determination of bandwidth plays an important role in the non-parametric cloud-KDE approach for seismic fragility. When changing the one-dimensional bandwidth, the smallest FAE for the four conditions in Fig. 13 is marked as 0.0246, 0.0211, 0.0081 and 0.0328, which is in consistency with the results in Figs. 12(c) and 12(d). When changing the two-dimensional bandwidth, the smallest FAE for the four conditions in Fig. 14 is also marked as 0.0246, 0.0211, 0.0081 and 0.0328, which is also in consistency with the results in Figs. 12(c) and 12(d). The conclusion indicates that the procedure to calculate the one-dimensional and two-dimensional bandwidth in Fig. 1 and Sec. 5 is optimal and effective, and the variation of bandwidth can result in a larger FAE and lower accuracy against the

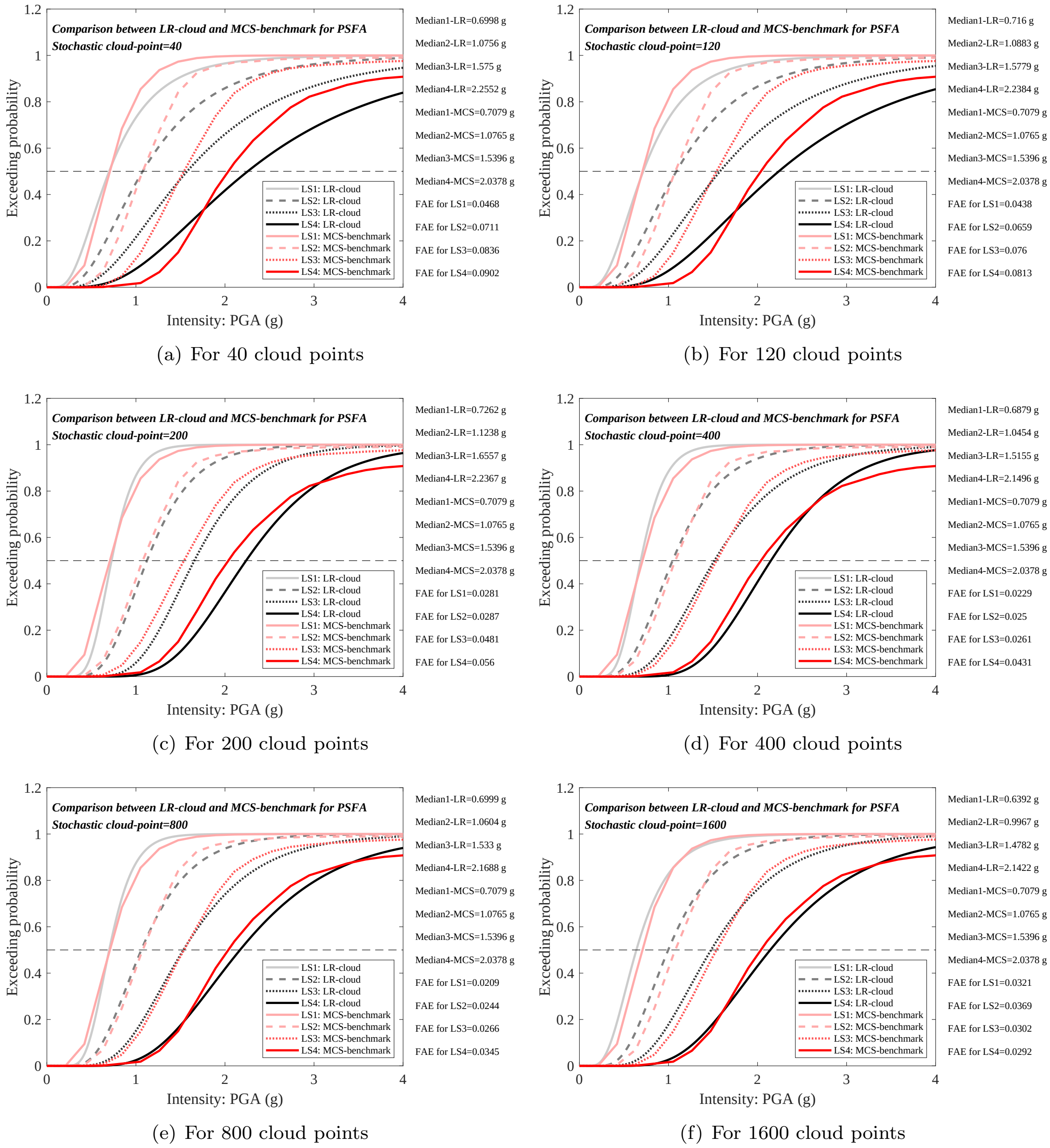


Figure 11: Comparison between the parametric cloud-LR approach and the benchmark cloud-MCS approach

benchmark cloud-MCS approach. The parametric analysis of intensity measure and bandwidth also provides some valuable insights for the further development of the non-parametric cloud-KDE approach for efficient seismic fragility assessment.

## 7. Conclusions

In this paper, a KDE-based non-parametric cloud approach is proposed for efficient seismic fragility estimation of structures under non-stationary excitation. First, the methodology framework of the efficient

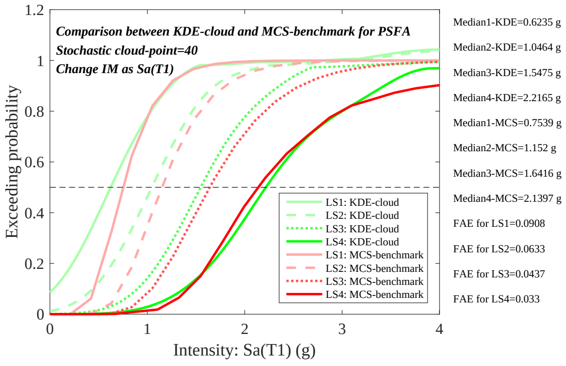


(a) For 40 cloud points (change PGA to $S_a(T_1)$)

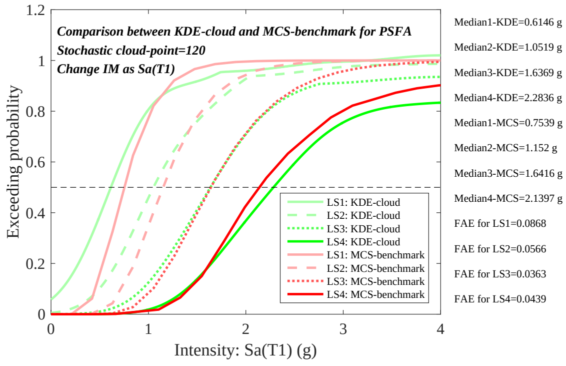


(b) For 120 cloud points (change PGA to $S_a(T_1)$)

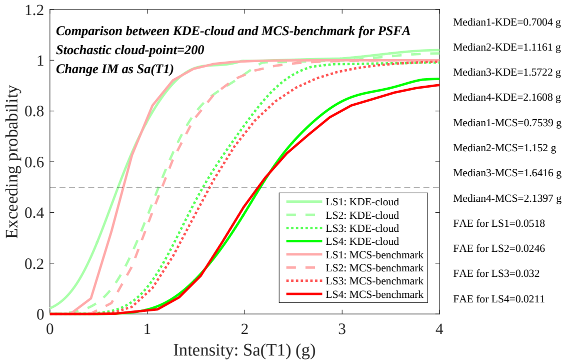


(c) For 200 cloud points (change PGA to $S_a(T_1)$)

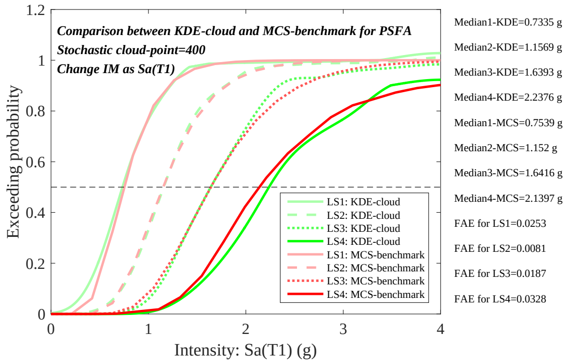


(d) For 400 cloud points (change PGA to $S_a(T_1)$)

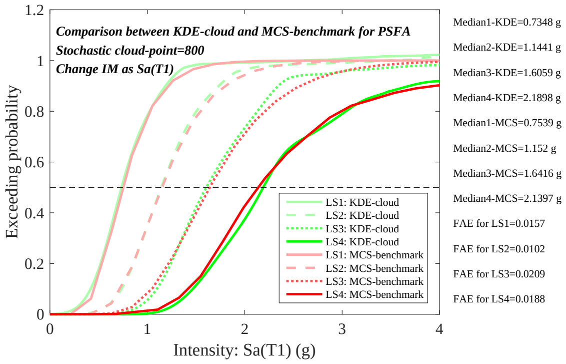


(e) For 800 cloud points (change PGA to $S_a(T_1)$)

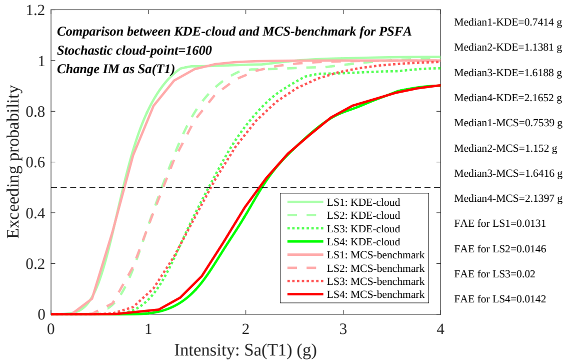


(f) For 1600 cloud points (change PGA to $S_a(T_1)$)

Figure 12: Parametric analysis of intensity measure in the non-parametric cloud-KDE approach [change PGA to $S_a(T_1)$]

approach is illustrated. Then, the procedures of non-stationary stochastic seismic response of structures and KDE-based non-parametric cloud approach for efficient seismic fragility are demonstrated. After that, an application example via a three-span-six-story RCF is given for implementation, followed with a parametric analysis of critical factors. During the process, the classic parametric cloud-LR approach and benchmark cloud-MCS approach are also incorporated for validation, from which the following conclusions may be drawn:

1. The non-stationary stochastic responses of structures reflect the stochastic properties and time-varying effects of earthquake excitations, and the adoption of non-stationary stochastic earthquakes can be

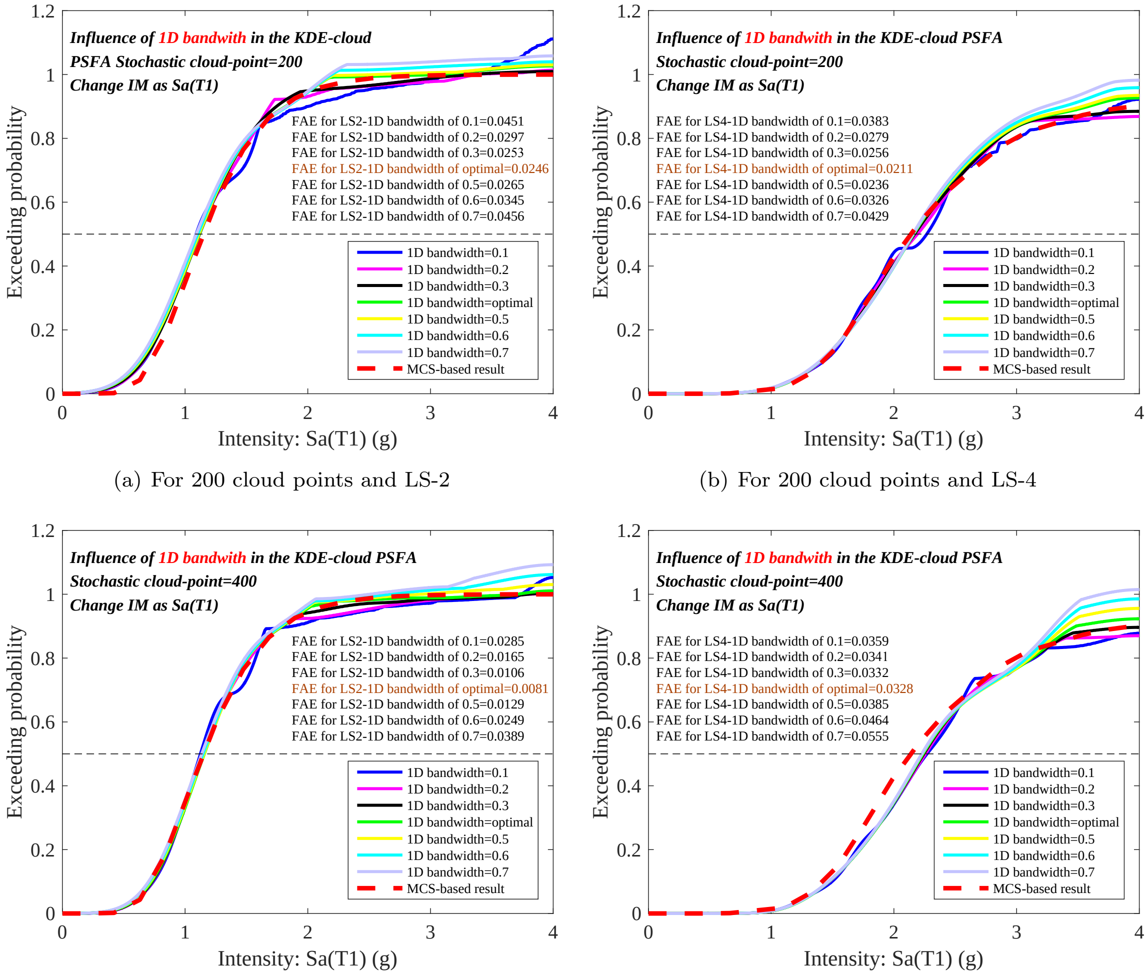


(a) For 200 cloud points and LS-2

(b) For 200 cloud points and LS-4

(c) For 400 cloud points and LS-2

(d) For 400 cloud points and LS-4

Figure 13: Parametric analysis of one-dimensional bandwidth in the non-parametric cloud-KDE approach

a more objective strategy for seismic fragility assessment of structures. At this stage, although the lognormal-based parametric assumption is classic in seismic fragility , it also indicates some limitations and constraints in actual analysis, thus a non-parametric approach to express the intrinsic seismic fragility may be more objective and real. The non-parametric KDE-based fragility approach is unique and superior for its pure analytical expression of fragility without any distribution assumptions. Most importantly, compared with the other non-parametric approaches, the KDE-based fragility approach indicates a great potential to connect with the cloud analysis approach in sample generations (i.e., cloud-KDE in this paper), which sharply reduces the calculating burdens and improves the analyzing efficiency. Thus, how to implement the non-parametric KDE-based approach for structural fragility assessment deserves attention, and in this paper, a framework of non-parametric cloud-KDE approach is proposed for the non-stationary stochastic seismic fragility assessment of structures. The methodology framework of the approach is introduced, and the procedures of non-stationary stochastic seismic response of structures and KDE-based non-parametric cloud approach for efficient seismic fragility are illustrated. From Secs. 2 to 4, the corresponding derived formulas demonstrate the feasibility and applicability of the KDE-based non-parametric cloud approach for fragility assessment in an analytical form.

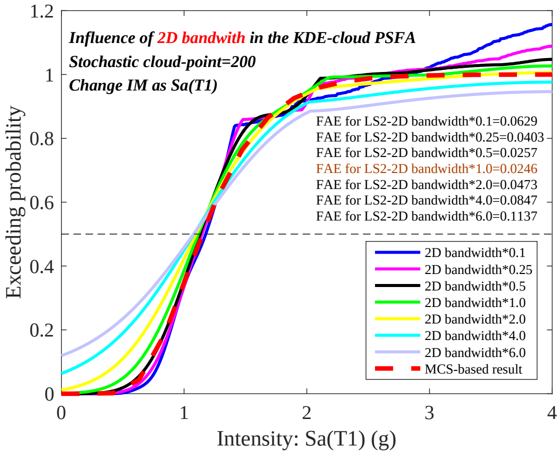


(a) For 200 cloud points and LS-2

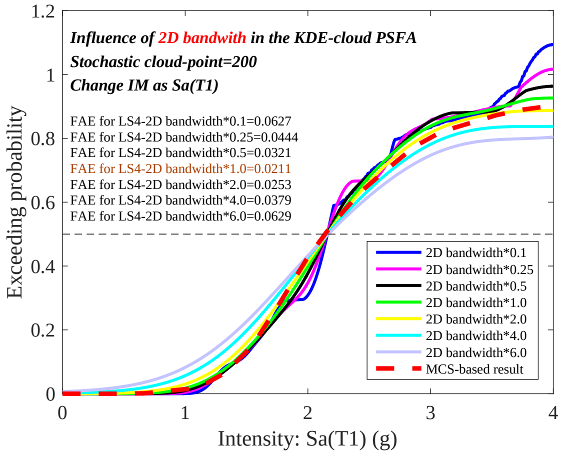


(b) For 200 cloud points and LS-4

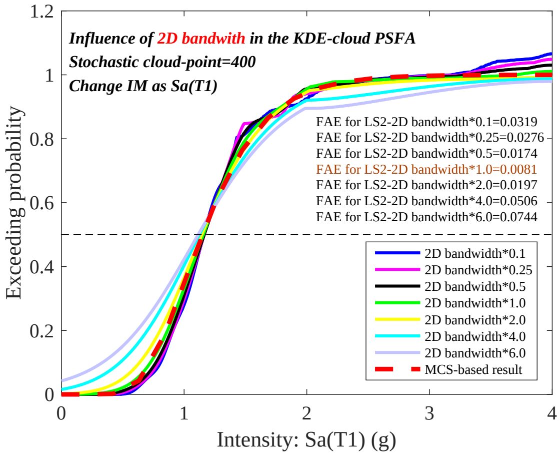


(c) For 400 cloud points and LS-2

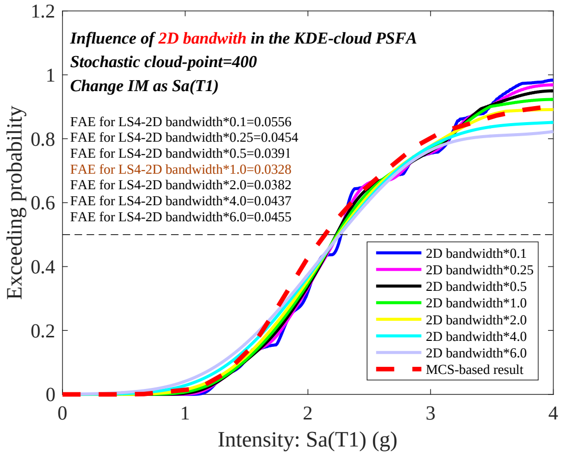


(d) For 400 cloud points and LS-4

Figure 14: Parametric analysis of two-dimensional bandwidth in the non-parametric cloud-KDE approach

2. An application example via a three-span-six-story RCF is given for illustration, and during the process, both the classic parametric cloud-LR approach and benchmark cloud-MCS approach are incorporated for validation and comparison. For both the cloud-LR and cloud-KDE approaches, the obtained seismic fragility curves show similar tendency with the cloud-MCS approach, and with the increase of cloud number, the corresponding fitting degree is more closer and indicates a better effect. The FAE drops for both cloud-LR and cloud-KDE approaches under all the four limit states, with an average reducing ratio of 75.33% (cloud-KDE) and 52.75% (cloud-LR), which indicates a greater fragility accuracy with the cloud number increasing. At the same time, the non-parametric cloud-KDE approach presents a comparable fragility with the benchmark cloud-MCS approach, and in most conditions, the cloud-KDE approach even shows less deviation in comparison with the classic parametric cloud-LR approach. For each cloud number condition, the average FAE of KDE-MCS is smaller than the LR-MCS, with the average dropping ratios of 31.05%, 37.40%, 51.96% and 59.19% from LS1 to LS4, respectively. In general, the analysis verifies the effectiveness of the non-parametric cloud-KDE approach without requiring more computation work (i.e., same as the parametric cloud-LR approach and much less than the benchmark cloud-MCS approach), and meanwhile it indicates a comparable accuracy with the classic fragility approaches (i.e., less deviation than the parametric cloud-LR approach and much

Table 6: Parametric analysis of bandwidth in the non-parametric cloud-KDE approach

| Change of bandwidth | 200 cloud points and LS-2 | 200 cloud points and LS-4 | 400 cloud points and LS-2 | 400 cloud points and LS-4 |
|---|---|---|---|---|
| One-dimensional bandwidth of 0.1 | 0.0451 | 0.0383 | 0.0285 | 0.0359 |
| One-dimensional bandwidth of 0.2 | 0.0297 | 0.0279 | 0.0165 | 0.0341 |
| One-dimensional bandwidth of 0.3 | 0.0253 | 0.0256 | 0.0106 | 0.0332 |
| One-dimensional bandwidth of optimal | 0.0246 | 0.0211 | 0.0081 | 0.0328 |
| One-dimensional bandwidth of 0.5 | 0.0265 | 0.0236 | 0.0129 | 0.0385 |
| One-dimensional bandwidth of 0.6 | 0.0345 | 0.0326 | 0.0249 | 0.0464 |
| One-dimensional bandwidth of 0.7 | 0.0456 | 0.0429 | 0.0389 | 0.0555 |
| Two-dimensional bandwidth of optimal × 0.1 | 0.0629 | 0.0627 | 0.0319 | 0.0556 |
| Two-dimensional bandwidth of optimal × 0.25 | 0.0403 | 0.0444 | 0.0276 | 0.0454 |
| Two-dimensional bandwidth of optimal × 0.5 | 0.0257 | 0.0321 | 0.0174 | 0.0391 |
| Two-dimensional bandwidth of optimal | 0.0246 | 0.0211 | 0.0081 | 0.0328 |
| Two-dimensional bandwidth of optimal × 2.0 | 0.0473 | 0.0253 | 0.0197 | 0.0382 |
| Two-dimensional bandwidth of optimal × 4.0 | 0.0847 | 0.0379 | 0.0506 | 0.0437 |
| Two-dimensional bandwidth of optimal × 6.0 | 0.1137 | 0.0629 | 0.0744 | 0.0455 |

closer to the benchmark cloud-MCS approach), which provides a new path for the development of non-stationary stochastic seismic fragility assessment via non-parametric approach.

3. A parametric analysis is further performed for the non-parametric cloud-KDE approach, and two critical factors that potentially influence the assessment result are elaborately discussed (i.e., the intensity measure and bandwidth). The intensity measure is first changed to $S_a(T_1)$ for comparison, and then the variations of both the one-dimensional and two-dimensional bandwidth are performed for discussion. In general, similar tendency between the non-parametric cloud-KDE approach and benchmark cloud-MCS approach is obtained via the measure of $S_a(T_1)$, which is in agreement with the conclusion via the measure of PGA. With the increase of stochastic cloud points, the FAE indicates a smaller value, which proves a better fitting accuracy against the benchmark cloud-MCS approach. The change of intensity measure shows little impact on the non-parametric cloud-KDE approach for seismic fragility, which demonstrates certain superiority than the classic parametric approach in a sense. The change of one-dimensional or two-dimensional bandwidth leads to obvious variations of the generated fragility curves, from both the perspective of fitting accuracy and curve smoothness. This also proves that the determination of bandwidth plays an important role in the non-parametric cloud-KDE approach for seismic fragility. The parametric analysis indicates that the procedure to calculate the bandwidth in Secs. 2 to 4 is optimal and effective, and the variation of bandwidth can result in a larger FAE and lower accuracy against the benchmark cloud-MCS approach. The parametric analysis of intensity measure and bandwidth provides some valuable insights for the further development of the non-parametric cloud-KDE approach for efficient seismic fragility assessment.

4. Some limitations are also listed herein for the further investigations. (1) Six scenarios (i.e., cloud points of 40, 120, 200, 400, 800 and 1600) are adopted in this analysis to validate the effectiveness and accuracy of the KDE-based non-parametric approach. As for determining the optimal value of stochastic cloud-point number, the corresponding discussions are not given in this paper. In the future work, a comprehensive performance index combining both the efficiency and accuracy in calculation can be proposed. (2) In the application example, only a RCF via the two-dimensional model is given to perform the KDE-based non-parametric fragility analysis, and in the future work, more complex structures with more detailed models (e.g., three-dimensional model considering spatial and torsional effects) can be adopted. (3) The intensity measures of PGA and $S_a(T_1)$ are both adopted in this analysis to verify the applicability of the KDE-based non-parametric approach. In the future work, more sophisticated intensity measures such as average spectral acceleration can be used for a more comprehensive analysis. (4) When the earthquake intensity is in a large level, the obtained results

may be deviated (e.g., for collapse cases) and the derived fragility curves may be affected (e.g., for LS-4). In the future work, the influence of these factors in the KDE-based non-parametric approach can be further investigated.

## Acknowledgements

The financial supports from the Project of National Key Research and Development Program of China (Grant No. 2022YFC3803004), the National Natural Science Foundation of China (Grant Nos. 52208164 and 52078119), the Natural Science Foundation of Jiangsu Province (Grant No. BK20220984), and the Bingtuan Science and Technology Program (No. 2023AB016-01) are greatly appreciated by the authors.

## References

[1] L. Eads, E. Miranda, D. G. Lignos, Average spectral acceleration as an intensity measure for collapse risk assessment, Earthquake Engineering & Structural Dynamics 44 (12) (2015) 2057–2073.

[2] M. Kohrangi, P. Bazzurro, D. Vamvatsikos, A. Spillatura, Conditional spectrum-based ground motion record selection using average spectral acceleration, Earthquake Engineering & Structural Dynamics 46 (10) (2017) 1667–1685.

[3] X.-Y. Cao, G. Wu, D.-C. Feng, Z. Wang, H.-R. Cui, Research on the seismic retrofitting performance of rc frames using sc-pbspc brbf substructures, Earthquake Engineering & Structural Dynamics 49 (8) (2020) 794–816.

[4] Y. Bai, Y. Ma, Q. Yang, J. Florez-Lopez, X. Li, F. Biondini, Earthquake-induced damage updating for remaining-life assessment of steel frame substructure systems, Mechanical Systems and Signal Processing 159 (2021) 107782.

[5] Z.-P. Chen, S. Zhu, H. Yu, B. Wang, Development of novel sma-based d-type self-centering eccentrically braced frames, Engineering Structures 260 (2022) 114228.

[6] S.-Z. Chen, S.-Y. Zhang, D.-C. Feng, E. Taciroglu, Embedding prior knowledge into data-driven structural performance prediction to extrapolation from training domains, Journal of Engineering Mechanics 10.1061/JENMDT/EMENG-7062 (2023).

[7] C. A. Cornell, F. Jalayer, R. O. Hamburger, D. A. Foutch, Probabilistic basis for 2000 sac federal emergency management agency steel moment frame guidelines, Journal of structural engineering 128 (4) (2002) 526–533.

[8] P. Gardoni, A. Der Kiureghian, K. M. Mosalam, Probabilistic capacity models and fragility estimates for reinforced concrete columns based on experimental observations, Journal of Engineering Mechanics 128 (10) (2002) 1024–1038.

[9] B. Möller, W. Graf, M. Beer, Safety assessment of structures in view of fuzzy randomness, Computers & Structures 81 (15) (2003) 1567–1582.

[10] G. Lupoi, P. Franchin, A. Lupoi, P. E. Pinto, Seismic fragility analysis of structural systems, Journal of Engineering Mechanics 132 (4) (2006) 385–395.

[11] G. P. Cimellaro, A. Reinhorn, Multidimensional performance limit state for hazard fragility functions, Journal of engineering mechanics 137 (1) (2011) 47–60.

[12] S. Hu, W. Wang, M. Shahria Alam, Comparative study on seismic fragility assessment of self-centering energy-absorbing dual rocking core versus buckling restrained braced systems under mainshock–aftershock sequences, Journal of Structural Engineering 147 (9) (2021) 04021124.

[13] O. Yazdanpanah, K. M. Dolatshahi, O. Moammer, Earthquake-induced economic loss estimation of eccentrically braced frames through roof acceleration-based nonmodel approach, Journal of Constructional Steel Research 187 (2021) 106888.

[14] X.-Y. Cao, D.-C. Feng, G. Wu, Y.-H. Zeng, Reusing & replacing performances of the ab-brb with thin-walled concrete-infilled steel shells, Thin-Walled Structures 157 (2020) 107069.

[15] S. Öncü-Davas, C. Alhan, Reliability of semi-active seismic isolation under near-fault earthquakes, Mechanical Systems and Signal Processing 114 (2019) 146–164.

[16] X.-Y. Cao, D.-C. Feng, G. Wu, Z. Wang, Experimental and theoretical investigations of the existing reinforced concrete frames retrofitted with the novel external sc-pbspc brbf sub-structures, Engineering Structures 256 (2022) 113982.

[17] D. Shen, M. Li, Q. Yang, C. Wen, C. Liu, J. Kang, X. Cao, Seismic performance of earthquake-damaged corroded reinforced concrete beam-column joints retrofitted with basalt fiber-reinforced polymer sheets, Structure and Infrastructure Engineering (2022) 1–17.

[18] L. Hu, M. Li, T. Yiliyaer, W. Gao, H. Wang, Strengthening of cracked dh36 steel plates by cfrp sheets under fatigue loading at low temperatures, Ocean Engineering 243 (2022) 110203.

[19] X.-Y. Cao, D. Shen, D.-C. Feng, C.-L. Wang, Z. Qu, G. Wu, Seismic retrofitting of existing frame buildings through externally attached sub-structures: State of the art review and future perspectives, Journal of Building Engineering 57 (2022) 104904.

[20] J. Shi, S. Sun, X. Cao, H. Wang, Pullout behaviors of basalt fiber-reinforced polymer bars with mechanical anchorages for concrete structures exposed to seawater, Construction and Building Materials 373 (2023) 130866.

[21] Q. Zhang, N. Pan, M. Meloni, D. Lu, J. Cai, J. Feng, Reliability analysis of radially retractable roofs with revolute joint clearances, Reliability Engineering & System Safety 208 (2021) 107401.

[22] F. Cui, H. Li, X. Dong, B. Wang, J. Li, H. Xue, M. Qi, Improved time-dependent seismic fragility estimates for deteriorating rc bridge substructures exposed to chloride attack, Advances in Structural Engineering 24 (3) (2021) 437–452.

[23] Z.-P. Chen, D.-C. Feng, X.-Y. Cao, K.-J. Ma, S. Zhu, G. Wu, Probabilistic seismic demand and fragility analysis of a novel mid-rise large-span cassette structure, Bulletin of Earthquake Engineering (2022) 1–31.
[24] Y. Lu, Y. Liu, Y. Wang, J. Liu, X. Huang, Development of a novel buckling-restrained damper with additional friction energy dissipation: Component tests and structural verification, Engineering Structures 274 (2023) 115188.
[25] Q. Shang, J. Li, C. Du, T. Wang, Seismic fragility analysis of freestanding hospital cabinets based on shaking table tests, Journal of Earthquake Engineering 27 (8) (2023) 1993–2012.
[26] L. Huang, B. Zeng, Z. Zhou, W. Zhang, Y. Wei, C. Li, Seismic behavior and reliability of variable friction damped self-centering prestressed concrete frames considering bolt bearing, Soil Dynamics and Earthquake Engineering 164 (2023) 107643.
[27] O. Yazdanpanah, K. M. Dolatshahi, O. Moammer, Rapid seismic fragility curves assessment of eccentrically braced frames through an output-only nonmodel-based procedure and machine learning techniques, Engineering Structures 278 (2023) 115290.
[28] X.-Y. Cao, D.-C. Feng, G. Wu, J.-G. Xu, Probabilistic seismic performance assessment of rc frames retrofitted with external sc-pbspc brbf sub-structures, Journal of Earthquake Engineering (2021) 1–24.
[29] J.-G. Xu, D.-C. Feng, S. Mangalathu, J.-S. Jeon, Data-driven rapid damage evaluation for life-cycle seismic assessment of regional reinforced concrete bridges, Earthquake Engineering & Structural Dynamics 51 (11) (2022) 2730–2751.
[30] Y. Lin, X. He, A. Igarashi, Influence of directionality of spectral-compatible bi-directional ground motions on critical seismic performance assessment of base-isolation structures, Earthquake Engineering & Structural Dynamics 51 (6) (2022) 1477–1500.
[31] Y. Lin, Y. Wang, W. Wu, S. Yang, Z. Guo, D. Guan, G. Li, Experimental study on pspc beam–concrete encased cfst column frame installed with novel steel panel dampers, Engineering Structures 288 (2023) 116211.
[32] A. K. Chopra, Dynamics of structures, Pearson Education India, 2007.
[33] M. K. Kaul, Stochastic characterization of earthquakes through their response spectrum, Earthquake Engineering & Structural Dynamics 6 (5) (1978) 497–509.
[34] S. Rezaeian, A. Der Kiureghian, Simulation of synthetic ground motions for specified earthquake and site characteristics, Earthquake Engineering & Structural Dynamics 39 (10) (2010) 1155–1180.
[35] F. Scozzese, E. Tubaldi, A. Dall'Asta, Assessment of the effectiveness of multiple-stripe analysis by using a stochastic earthquake input model, Bulletin of Earthquake Engineering 18 (7) (2020) 3167–3203.
[36] E. H. Vanmarcke, E. Heredia-Zavoni, G. A. Fenton, Conditional simulation of spatially correlated earthquake ground motion, Journal of Engineering Mechanics 119 (1993) 2333–2333.
[37] O. Matania, R. Klein, J. Bortman, Algorithms for spectrum background estimation of non-stationary signals, Mechanical Systems and Signal Processing 167 (2022) 108551.
[38] D.-C. Feng, X.-Y. Cao, D. Wang, G. Wu, A pdem-based non-parametric seismic fragility assessment method for rc structures under non-stationary ground motions, Journal of Building Engineering (2022) 105465.
[39] X.-Y. Cao, D.-C. Feng, M. Beer, Consistent seismic hazard and fragility analysis considering combined capacity-demand uncertainties via probability density evolution method, Structural Safety 103 (2023) 102330.
[40] B. Peng, J. Xu, Y. Peng, Efficient simulation of multivariate non-stationary ground motions based on a virtual continuous process and eole, Mechanical Systems and Signal Processing 184 (2023) 109722.
[41] J.-G. Xu, X.-Y. Cao, J. Shi, Z. Wang, A comparative study of the novel externally-attached precast src braced-frames for seismic retrofitting under near-field spectrum-compatible non-stationary stochastic earthquake, in: Structures, Vol. 50, Elsevier, 2023, pp. 200–214.
[42] M. Amin, A. H.-S. Ang, Nonstationary stochastic models of earthquake motions, Journal of the Engineering Mechanics Division 94 (2) (1968) 559–584.
[43] M. Srinivasan, R. Corotis, B. Ellingwood, Generation of critical stochastic earthquakes, Earthquake engineering & structural dynamics 21 (4) (1992) 275–288.
[44] J. Conte, B. Peng, Fully nonstationary analytical earthquake ground-motion model, Journal of Engineering Mechanics 123 (1) (1997) 15–24.
[45] J. P. Stewart, S.-J. Chiou, J. D. Bray, R. W. Graves, P. G. Somerville, N. A. Abrahamson, Ground motion evaluation procedures for performance-based design, Soil dynamics and earthquake engineering 22 (9-12) (2002) 765–772.
[46] G. P. Mavroeidis, A. S. Papageorgiou, A mathematical representation of near-fault ground motions, Bulletin of the seismological society of America 93 (3) (2003) 1099–1131.
[47] F. Jalayer, J. Beck, Effects of two alternative representations of ground-motion uncertainty on probabilistic seismic demand assessment of structures, Earthquake engineering & structural dynamics 37 (1) (2008) 61–79.
[48] I. Gidaris, A. A. Taflanidis, G. P. Mavroeidis, Kriging metamodeling in seismic risk assessment based on stochastic ground motion models, Earthquake Engineering & Structural Dynamics 44 (14) (2015) 2377–2399.
[49] N. S. Kwong, A. K. Chopra, R. K. McGuire, Evaluation of ground motion selection and modification procedures using synthetic ground motions, Earthquake Engineering & Structural Dynamics 44 (11) (2015) 1841–1861.
[50] B. R. Ellingwood, D. V. Rosowsky, Y. Li, J. H. Kim, Fragility assessment of light-frame wood construction subjected to wind and earthquake hazards, Journal of Structural Engineering 130 (12) (2004) 1921–1930.
[51] D.-E. Choe, P. Gardoni, D. Rosowsky, Closed-form fragility estimates, parameter sensitivity, and bayesian updating for rc columns, Journal of engineering mechanics 133 (7) (2007) 833–843.
[52] D. Straub, A. Der Kiureghian, Bayesian network enhanced with structural reliability methods: Application, Journal of Engineering Mechanics 136 (10) (2010) 1259–1270.
[53] M. Beer, M. Liebscher, Designing robust structures–a nonlinear simulation based approach, Computers & Structures 86 (10) (2008) 1102–1122.

[54] I. P. Mitseas, M. Beer, Fragility analysis of nonproportionally damped inelastic mdof structural systems exposed to stochastic seismic excitation, Computers & Structures 226 (2020) 106129.
[55] B. G. Nielson, R. DesRoches, Seismic fragility methodology for highway bridges using a component level approach, Earthquake engineering & structural dynamics 36 (6) (2007) 823–839.
[56] J. Ghosh, J. E. Padgett, Aging considerations in the development of time-dependent seismic fragility curves, Journal of Structural Engineering 136 (12) (2010) 1497–1511.
[57] I. Zentner, M. Gündel, N. Bonfils, Fragility analysis methods: Review of existing approaches and application, Nuclear Engineering and design 323 (2017) 245–258.
[58] K. Bakalis, D. Vamvatsikos, Seismic fragility functions via nonlinear response history analysis, Journal of structural engineering 144 (10) (2018) 04018181.
[59] M. A. Hariri-Ardebili, V. E. Saouma, Seismic fragility analysis of concrete dams: A state-of-the-art review, Engineering Structures 128 (2016) 374–399.
[60] X.-Y. Cao, D.-C. Feng, G. Wu, Seismic performance upgrade of rc frame buildings using precast bolt-connected steel-plate reinforced concrete frame-braces, Engineering Structures 195 (2019) 382 – 399.
[61] H. Li, L. Li, W. Wu, L. Xu, Seismic fragility assessment framework for highway bridges based on an improved uniform design-response surface model methodology, Bulletin of Earthquake Engineering 18 (5) (2020) 2329–2353.
[62] S. Hu, S. Zhu, Life-cycle benefits estimation for hybrid seismic-resistant self-centering braced frames, Earthquake Engineering & Structural Dynamics (2023).
[63] A. Karamlou, P. Bocchini, Computation of bridge seismic fragility by large-scale simulation for probabilistic resilience analysis, Earthquake Engineering & Structural Dynamics 44 (12) (2015) 1959–1978.
[64] B. Bradley, R. Dhakal, M. Cubrinovski, G. A. MacRae, D. S. Lee, Seismic loss estimation for efficient decision making (2008).
[65] S. Mangalathu, J.-S. Jeon, Stripe-based fragility analysis of multispan concrete bridge classes using machine learning techniques, Earthquake Engineering & Structural Dynamics 48 (11) (2019) 1238–1255.
[66] R. Capillon, C. Desceliers, C. Soize, Uncertainty quantification in computational linear structural dynamics for viscoelastic composite structures, Computer Methods in Applied Mechanics and Engineering 305 (2016) 154–172.
[67] D.-C. Feng, X.-Y. Cao, M. Beer, An enhanced pdem-based framework for reliability analysis of structures considering multiple failure modes and limit states, Probabilistic Engineering Mechanics 70 (2022) 103367.
[68] X.-Y. Cao, D.-C. Feng, Y. Li, Assessment of various seismic fragility analysis approaches for structures excited by non-stationary stochastic ground motions, Mechanical Systems and Signal Processing 186 (2023) 109838.
[69] D. Lallemant, A. Kiremidjian, H. Burton, Statistical procedures for developing earthquake damage fragility curves, Earthquake Engineering & Structural Dynamics 44 (9) (2015) 1373–1389.
[70] K. Trevlopoulos, C. Feau, I. Zentner, Parametric models averaging for optimized non-parametric fragility curve estimation based on intensity measure data clustering, Structural Safety 81 (2019) 101865.
[71] R. Gentile, C. Galasso, Gaussian process regression for seismic fragility assessment of building portfolios, Structural Safety 87 (2020) 101980.
[72] D. Altieri, E. Patelli, An efficient approach for computing analytical non-parametric fragility curves, Structural Safety 85 (2020) 101956.
[73] F. Jalayer, C. Cornell, Alternative non-linear demand estimation methods for probability-based seismic assessments, Earthquake Engineering & Structural Dynamics 38 (8) (2009) 951–972.
[74] A. Naess, B. Leira, O. Batsevych, System reliability analysis by enhanced monte carlo simulation, Structural safety 31 (5) (2009) 349–355.
[75] B. Echard, N. Gayton, M. Lemaire, Ak-mcs: an active learning reliability method combining kriging and monte carlo simulation, Structural Safety 33 (2) (2011) 145–154.
[76] J. W. Baker, Efficient analytical fragility function fitting using dynamic structural analysis, Earthquake Spectra 31 (1) (2015) 579–599.
[77] S. Mangalathu, J.-S. Jeon, J. E. Padgett, R. DesRoches, Performance-based grouping methods of bridge classes for regional seismic risk assessment: Application of anova, ancova, and non-parametric approaches, Earthquake Engineering & Structural Dynamics 46 (14) (2017) 2587–2602.
[78] S. Lee, Monte carlo simulation using support vector machine and kernel density for failure probability estimation, Reliability Engineering & System Safety 209 (2021) 107481.
[79] S. Ghosh, A. Roy, S. Chakraborty, Kriging metamodeling-based monte carlo simulation for improved seismic fragility analysis of structures, Journal of Earthquake Engineering 25 (7) (2021) 1316–1336.
[80] I. Iervolino, Estimation uncertainty for some common seismic fragility curve fitting methods, Soil Dynamics and Earthquake Engineering 152 (2022) 107068.
[81] G. R. Terrell, D. W. Scott, Variable kernel density estimation, The Annals of Statistics (1992) 1236–1265.
[82] I. Takewaki, Nonstationary random critical excitation for nonproportionally damped structural systems, Computer methods in applied mechanics and engineering 190 (31) (2001) 3927–3943.
[83] Z. Liu, Z. Liu, Random function representation of stationary stochastic vector processes for probability density evolution analysis of wind-induced structures, Mechanical Systems and Signal Processing 106 (2018) 511–525.
[84] F. Kong, Y. Zhang, Y. Zhang, Non-stationary response power spectrum determination of linear/non-linear systems endowed with fractional derivative elements via harmonic wavelet, Mechanical Systems and Signal Processing 162 (2022) 108024.
[85] X.-Y. Cao, An iterative psd-based procedure for the gaussian stochastic earthquake model with combined intensity and frequency nonstationarities: Its application into precast concrete structures, Mathematics 11 (6) (2023) 1294.

[86] R. Clough, J. Penzien, Dynamics of Structures, McGraw-Hill, 1975.
[87] M. Shinozuka, G. Deodatis, Simulation of multi-dimensional gaussian stochastic fields by spectral representation (1996).
[88] R. Pang, Y. Zhou, G. Chen, M. Jing, D. Yang, Stochastic mainshock–aftershock simulation and its applications in dynamic reliability of structural systems via dpim, Journal of Engineering Mechanics 149 (1) (2022) 04022096.
[89] Z. Liu, W. Liu, Y. Peng, Random function based spectral representation of stationary and non-stationary stochastic processes, Probabilistic Engineering Mechanics 45 (2016) 115–126.
[90] G. Deodatis, Non-stationary stochastic vector processes: seismic ground motion applications, Probabilistic engineering mechanics 11 (3) (1996) 149–167.
[91] Z. Liu, B. Zeng, L. Wu, Spectral representation of non-stationary ground motion process simulation: Random function method (in chinese), Journal of Vibration Engineering 28 (3) (2015) 411–417.
[92] C. Mai, K. Konakli, B. Sudret, Seismic fragility curves for structures using non-parametric representations, Frontiers of Structural and Civil Engineering 11 (2) (2017) 169–186.
[93] M. P. Wand, M. C. Jones, Kernel smoothing, CRC press, 1994.
[94] T. Duong, et al., ks: Kernel density estimation and kernel discriminant analysis for multivariate data in r, Journal of Statistical Software 21 (7) (2007) 1–16.
[95] R. Zhang, H. Dai, Stochastic analysis of structures under limited observations using kernel density estimation and arbitrary polynomial chaos expansion, Computer Methods in Applied Mechanics and Engineering 403 (2023) 115689.
[96] J. Xu, D.-C. Feng, Seismic response analysis of nonlinear structures with uncertain parameters under stochastic ground motions, Soil Dynamics and Earthquake Engineering 111 (2018) 149–159.
[97] X.-Y. Cao, D.-C. Feng, G. Wu, Pushover-based probabilistic seismic capacity assessment of rcfs retrofitted with pbspc brbf sub-structures, Engineering Structures 234 (2021) 111919.
[98] D.-C. Feng, S.-C. Xie, J. Xu, K. Qian, Robustness quantification of reinforced concrete structures subjected to progressive collapse via the probability density evolution method, Engineering Structures 202 (2020) 109877.
[99] X. Yu, Probabilistic seismic fragility and risk analysis of reinforced concrete frame structures, Ph.D thesis of Harbin Institute of Technology, China (2010).
[100] M. Barbato, Q. Gu, J. Conte, Probabilistic push-over analysis of structural and soil-structure systems, Journal of structural engineering 136 (11) (2010) 1330–1341.
[101] F. McKenna, G. L. Fenves, M. H. Scott, et al., Open system for earthquake engineering simulation, University of California, Berkeley, CA (2000).
[102] D.-C. Feng, Z. Wang, X.-Y. Cao, G. Wu, Damage mechanics-based modeling approaches for cyclic analysis of precast concrete structures: A comparative study, International Journal of Damage Mechanics 29 (6) (2020) 965–987.
[103] J.-G. Xu, X.-Y. Cao, G. Wu, Seismic collapse and reparability performance of reinforced concrete frames retrofitted with external pbspc brbf sub-frame in near-fault regions, Journal of Building Engineering 64 (2023) 105716.
[104] X.-Y. Cao, D.-C. Feng, C.-L. Wang, D. Shen, G. Wu, A stochastic csm-based displacement-oriented design strategy for the novel precast src-uhpc composite braced-frame in the externally attached seismic retrofitting, Composite Structures 321 (2023) 117308.
[105] B. D. Scott, R. Park, M. Priestley, Stress-strain behavior of concrete confined by overlapping hoops at low and high strain rates, Journal Proceedings 79 (1) (1982) 13–27.
[106] E. C. Bentz, Sectional analysis of reinforced concrete members, Ph.D. thesis, University of Toronto, Canada (2000).
[107] X.-Y. Cao, C.-Z. Xiong, D.-C. Feng, G. Wu, Dynamic and probabilistic seismic performance assessment of precast prestressed reinforced concrete frames incorporating slab influence through three-dimensional spatial model, Bulletin of Earthquake Engineering (2022) 1–35.
[108] X.-Y. Cao, G. Wu, J.-W. W. Ju, Seismic performance improvement of existing rcfs using external pt-pbspc frame substructures: Experimental verification and numerical investigation, Journal of Building Engineering 46 (2022) 103649.
[109] Z. Wang, D.-C. Feng, X. Cao, G. Wu, Seismic performance assessment of code-conforming precast reinforced concrete frames in china, Earthquakes and Structures 21 (3) (2021) 277.
[110] GB50011, Code for seismic design of buildings (gb50011) (2010).
[111] M. Grigoriu, To scale or not to scale seismic ground-acceleration records, Journal of engineering mechanics 137 (4) (2011) 284–293.
[112] F. Jalayer, J. Beck, F. Zareian, Analyzing the sufficiency of alternative scalar and vector intensity measures of ground shaking based on information theory, Journal of Engineering Mechanics 138 (3) (2012) 307–316.
[113] F. Di Trapani, L. Giordano, G. Mancini, Progressive collapse response of reinforced concrete frame structures with masonry infills, Journal of Engineering Mechanics 146 (3) (2020) 04020002.
[114] L. Micheli, L. Cao, S. Laflamme, A. Alipour, Life-cycle cost evaluation strategy for high-performance control systems under uncertainties, Journal of Engineering Mechanics 146 (2) (2020) 04019134.
[115] O. C. Celik, B. R. Ellingwood, Seismic fragilities for non-ductile reinforced concrete frames–role of aleatoric and epistemic uncertainties, Structural Safety 32 (1) (2010) 1–12.
[116] X.-Y. Cao, G. Wu, D.-C. Feng, X.-J. Zu, Experimental and numerical study of outside strengthening with precast bolt-connected steel plate–reinforced concrete frame-brace, Journal of Performance of Constructed Facilities 33 (6) (2019) 04019077.
[117] X.-Y. Cao, D.-C. Feng, Z. Wang, G. Wu, Parametric investigation of the assembled bolt-connected buckling-restrained brace and performance evaluation of its application into structural retrofit, Journal of Building Engineering (2022) 103988.
[118] Z. Fang, L. Hu, H. Jiang, S. Fang, G. Zhao, Y. Ma, Shear performance of high-strength friction-grip bolted shear connector in prefabricated steel–uhpc composite beams: Finite element modelling and parametric study, Case Studies in Construction Materials 18 (2023) e01860.

[119] E. Bojórquez, I. Iervolino, A. Reyes-Salazar, S. E. Ruiz, Comparing vector-valued intensity measures for fragility analysis of steel frames in the case of narrow-band ground motions, Engineering Structures 45 (2012) 472–480.
[120] K. E. Bantilas, I. E. Kavvadias, L. K. Vasiliadis, A. Elenas, Seismic fragility and intensity measure investigation for rocking podium structures under synthetic pulse-like excitations, Earthquake Engineering & Structural Dynamics 50 (13) (2021) 3441–3459.